2026-06

Kinetic Monte Carlo-Guided Green Synthesis and Theoretical Investigation of Zno Nanoparticles for Solar Cell Efficiency Enhancement

Natinael, Tezana

BAHIR DAR UNIVERSITY

DEPARTMENT OF PHYSICS

KINETIC MONTE CARLO-GUIDED GREEN SYNTHESIS AND THEORETICAL INVESTIGATION OF ZNO NANOPARTICLES FOR SOLAR CELL EFFICIENCY ENHANCEMENT

By

Natinael Tezana

***A*dvisor: Dr. Getachew Tizazu (Asso.Professor)**

A thesis submitted to Bahir Dar University, Department of Physics

In partial fulfilment of the requirements for Masters of Science In

Semiconductor Physics

June, 2026

Bahir Dar, Ethiopia

As members of the examining committee of the final M.Sc. thesis open defense, this is to certify that the thesis prepared by **Natinael Tezana** entitled **"Kinetic Monte Carlo-Guided Green Synthesis And Theoretical Investigation Of ZnO Nanoparticles For Solar Cell Efficiency Enhancement"** complies with the regulations of the university and meets the accepted requirements for the degree of Master of Science in Semiconductor Physics.

Approved by the Examining Committee:

Advisor	**Signature**	**Date**
Getachew Tizazu (PhD)	_____	_____
Chair Person		
_____	_____	_____
Internal Examiner		
_____	_____	_____
External Examiner		
_____	_____	_____

DECLARATION

I, the undersigned, declare that this thesis entitled **"Kinetic Monte Carlo-Guided Green Synthesis And Theoretical Investigation Of ZnO Nanoparticles For Solar Cell Efficiency Enhancement"** is my original work with the guidance of my advisors,and has not been presented by any other person for an award of a degree in Bahir Dar University or any other University, and that all resources of materials used for this study have been duly acknowledged.

Natinael Tezana _____ _____

Signature *Date*

ACKNOWLEDGEMENT

First and foremost, I would like to express my deepest gratitude to Almighty God for giving me strength, patience, wisdom, and guidance throughout the completion of this thesis.

I would like to extend my sincere appreciation to my advisor, Dr.Getachew Tizazu, for the continuous guidance, valuable suggestions, constructive comments, and encouragement provided during every stage of this research work. His support and academic insight greatly contributed to the successful completion of this thesis.

I would like to express my sincere appreciation to Dr. Amare Benor from Bahir Dar University for allowing me to use the laboratory facilities during the experimental work of this research.

I also highly acknowledge Prof. Marc Burgelman and his research team at the Department of Electronics and Information Systems (ELIS), Ghent University, Belgium, for developing and freely providing the SCAPS-1D software package used to numerically model our solar cell architectures.

My heartfelt thanks also goes to my Mom for her endless love, moral support, encouragement, and sacrifices. Her confidence in me has always been a source of motivation and strength.

Finally, I wish to acknowledge all individuals who directly or indirectly contributed to the successful completion of this thesis.

Dedication

This work is dedicated to My Beloved mother Tiruye Assefa

TABLE OF CONTENTS

LIST OF FIGURES:

LIST OF TABLES:

LIST OF ACRONYMS AND ABBREVIATIONS

EDX: Energy Dispersive X-ray Spectroscopy

Eg: Optical Bandgap

EMM: Effective Mass Model

ETL: Electron Transport Layer

FTIR: Fourier Transform Infrared Spectroscopy

FTO: Fluorine-doped Tin Oxide

HCl: Hydrochloric acid

HTL: Hole Transport Layer

ITO: Indium Tin Oxide

M: Molar

NaOH: Sodium Hydrohydroxide

PSCs: Perovskite Solar Cells

rpm: Revolutions per minute

SEM: Scanning Electron Microscopy

SPR: Surface Plasmon Resonance

TCO: Transparent Conducting Oxide

UV-Vis: Ultraviolet-Visible Spectroscopy

XRD: X-Ray Diffraction

ZnO NPs: Zinc Oxide Nanoparticles

ZnO-Ag NCs: Zinc Oxide-Silver Nanocomposites

ABSTRACT

This study evaluates the influence of *Ocimum lamiifolium* leaf extract (OLE) concentration on the green synthesis of zinc oxide nanoparticles (ZnO NPs) and their performance as an Electron Transport Layer (ETL) in perovskite solar cells (PSCs). Synthesized across five extract-to-precursor ratios (1:2 to 3:2), the ZnO NPs followed a parabolic size trend dictated by competitive Ostwald ripening and steric crowding kinetics, which were modeled using atomistic Kinetic Monte Carlo (kMC) simulations. The 2:2 ratio achieved optimal stoichiometric equilibrium, yielding highly stable, pure nanoparticles with a 3.19 eV optical bandgap. This sample demonstrated an experimental crystalline core size of 10.80 nm (XRD) and an optical confinement size of 12.10 nm (Effective Mass Model), aligning exceptionally well with the kMC prediction of 10.24 nm (18.16% difference). EDX confirmed high purity with a minor 2.04 wt.% carbon signature from biomolecular capping. SCAPS-1D photovoltaic simulations proved that using this optimized ZnO (2:2) sample as an ultra-thin 20 nm ETL minimizes interfacial recombination and resistance, achieving a peak power conversion efficiency (PCE) of 16.03% (Jsc = 23.93 mA/cm^2, Voc = 1.11V). Increasing the ETL thickness to 90 nm systematically degraded performance due to bulk carrier trapping. This work highlights kMC validated, biogenic ZnO as a sustainable, efficient architecture for next-generation PSCs.

Keywords: Green Synthesis, Kinetic Monte Carlo, Zinc Oxide Nanoparticles, SCAPS-1D.

1. INTRODUCTION

1.1. Back Ground of The Study

Nanotechnology is the science and engineering concerned with the control, manipulation, restructuring, and understanding of matter at dimensions typically in the range of 1–100 nm, where materials exhibit unique size-dependent physical, chemical, optical, and electronic properties that differ significantly from their bulk counterparts [1]. At this nanoscale, phenomena such as quantum confinement, enhanced surface-to-volume ratio, and modified interatomic interactions lead to fundamentally new functionalities, enabling the development of advanced materials for applications in electronics, medicine, energy conversion, catalysis, and environmental remediation [2].

Nanotechnology generally follows two primary strategies for manipulating matter at the nanoscale: (i) the **top-down approach** and (ii) the **bottom-up approach**. In the *top-down approach*, bulk materials are gradually reduced to nanoscale dimensions using physical or mechanical techniques such as lithography, etching, and high-energy milling. Although this method is compatible with large-scale industrial fabrication, it often lacks precise atomic-level control and may introduce structural defects, resulting in nanomaterials that largely retain the properties of their bulk precursors [3].

In contrast, the *bottom-up approach*, also referred to as molecular nanotechnology, involves the construction of nanostructures from atoms, ions, or molecules through chemical synthesis, self-assembly, or biological processes. This approach offers superior control over particle size, morphology, composition, and surface chemistry, leading to highly uniform and functional nanomaterials. Bottom-up techniques are widely employed in the synthesis of nanoparticles, nanowires, and nanocomposites, and are particularly advantageous for tailoring material properties for specific applications [4,5].

Nanoparticles, which are defined as materials with dimensions in the range of 1-100 nm, are known for their unique physicochemical properties, which are quite different from their bulk counterparts due to significant size effects [6]. When materials are miniaturized to the nanoscale, the percentage of atoms present at the surface is considerably greater compared to the atoms

present inside the material. Due to the high surface energy, the ability of the material to adsorb, and its reactivity[7,8], the melting point of the material is decreased, the mechanical properties are altered, the catalytic activity is enhanced, and the interaction with the surrounding media is increased compared to the bulk material[9,10].

When materials are miniaturized to the nanoscale, the electronic properties of the materials are also significantly altered. In bulk materials, the electronic states are present in the form of energy bands, whereas at the nanoscale, the electronic states are discretized due to the presence of quantum confinement effects, which occur at sizes close to the exciton Bohr radius[11,12]. Due to these effects, the energy gap is varied by changing the sizes of the materials. Due to the discretized energy levels, the optical properties of the materials can be varied by changing the sizes of the materials[13.14]. Size-controlled optical properties of materials are quite significant in the field of optoelectronics, photodetectors, light-emitting devices, and photocatalysts. Moreover, the electrical conductivity of the materials is also altered at the nanoscale[15,16].

Among the variety of nanomaterials available, metal oxide and semiconductor nanoparticles have been of particular interest due to their chemical stability, abundance, eco-friendly nature, and multiple functionality. Zinc oxide (ZnO) nanoparticles have been one of the most studied semiconductor nanomaterials due to their large band gap (~3.37 eV) and exciton binding energy (~60 meV), which facilitate excitonic emission at room temperature [16,17]. Zinc oxide also possesses excellent photocatalytic activity, antimicrobial ability, UV absorption capability, and gas sensing ability, making it suitable for applications in the environment, cosmetics, solar cells, and optoelectronics [16,18,19].

The properties of ZnO nanoparticles vary significantly with the synthesis parameters due to the influence of size, shape, crystallite size, defects on the surface, and synthesis approaches. During the synthesis of ZnO nanoparticles, the synthesis parameters may vary due to the influence of nucleation and growth mechanisms, resulting in the synthesis of a variety of nanostructures such as nanorods, nanoflowers, nanospheres, and nanowires [20,21]. Defects on the surface of the ZnO nanoparticles play a crucial role in determining the photocatalytic as well as antimicrobial activities of the nanoparticles [14,22]. Furthermore, the size of the nanoparticles also plays an

important role in determining the band gap of the nanoparticles, which is crucial in determining the photocatalytic as well as optoelectronic activities of the nanoparticles [15,23].

Nanoparticles are broadly classified as organic, inorganic, and semiconductor types of nanomaterials. Organic nanoparticles, such as carbon-based nanostructures and polymeric nanoparticles, are widely used in various biomedical applications owing to their biocompatibility, biodegradability, and ability to control drug release [24,25]. Inorganic nanoparticles include various types of magnetic nanoparticles, noble metal nanoparticles, and metal oxide nanoparticles, which are highly valued for their structural robustness and functional versatility. Semiconductor nanoparticles such as TiO2 and ZnO nanoparticles are of significant interest in various photocatalytic and alternative energy-related applications owing to their adjustable electronic band structures and high surface reactivity [26,27].

Overall, the unique size-related structural, electronic, and surface-related properties of nanomaterials, as well as the progress made in the field of nanoparticle synthesis and characterization techniques, continue to expand the technological potential of these materials. A detailed understanding of the effects of nanoparticle size, shape, and surface characteristics on nanoparticle properties is of prime importance for optimizing nanoparticle performance in various technological applications [6,20, 23].

In the recent past, environmentally friendly "green synthesis" methods using plant extracts have garnered considerable research attention as viable alternatives to the conventional chemical synthesis of nanoparticles. The "plant-mediated synthesis" method uses bioactive compounds present in the plant extracts as natural reducing and stabilizing agents for the synthesis of nanoparticles of desired size and shape, while avoiding the formation of harmful byproducts.

Perovskite solar cells (PSCs) have emerged as the most promising research direction for the development of the next generation of solar cell devices owing to the superior power conversion efficiency, solution processability, and cost-effectiveness of the PSCs. Recent reviews on PSCs reveal the potential for improving the optical absorption, light management, and charge extraction using nanoparticles for the development of PSCs through the "near-field" and "far-field" enhancement mechanisms [28]. The incorporation of nanoparticles into the PSCs has been

shown to improve the optical absorption over the entire range of the solar spectrum and improve the overall performance of the PSCs[29,30]. The experimental and theoretical studies on the optical absorption of PSCs using nanoparticles also reveal the importance of the size, shape, and concentration of the nanoparticles for the optical absorption process[31,32].

1.2. Statement of The Problem

Zinc oxide nanoparticles (ZnO NPs) are widely utilized in optoelectronics and perovskite solar cells (PSCs) due to their superior optical bandgap and high electron mobility [33]. However, conventional physical and chemical synthesis methods demand high energy thresholds, costly infrastructure, and hazardous reagents that generate toxic secondary effluents [34,35]. While biogenic synthesis leveraging plant extracts offers an eco-friendly alternative, the structural optimization of these green precursors remains unstandardized. When utilizing extracts from indigenous flora like *Ocimum lamiifolium*, the exact volumetric extract-to-precursor ratio dictates the underlying reaction kinetics [36]. Unoptimized extraction matrices alter localized nucleation and crystal growth rates, causing high particle polydispersity and uncontrolled agglomeration that ultimately degrades electrical performance [37–39].

A prominent research gap in previous literature is that earlier works frequently treat plant extract volumes as static parameters, completely ignoring the non-linear morphological and thermodynamic shifts that occur when systematically varying precursor-to-extract ratios. Furthermore, earlier studies rely heavily on qualitative, trial-and-error empirical processing; there is a critical lack of atomistic-level theoretical modeling to explain the underlying thermodynamics of biogenic surface growth or to justify *why* specific stoichiometric nodes minimize particle size. Additionally, existing PSC device simulations almost exclusively utilize parameters from conventional sol-gel or chemical-vapor-deposited ZnO, completely ignoring the unique dielectric boundaries and localized strain profiles introduced by organic plant-extract capping monolayers [40,41]. This creates a severe disconnect between raw green synthesis configurations and predictive computational models, leaving the explicit link between plant extraction chemistry and macroscopic thin-film solar cell performance unmapped.

To address these limitations, this study introduces an integrated experimental and computational framework. A stochastic Kinetic Monte Carlo (kMC) simulation framework is developed to predict atomistic growth kinetics as a function of the extract matrix, directly validating the results against experimental X-ray Diffraction (XRD) core sizes and optical Effective Mass Model (EMM) boundaries. The validated parameters from the optimized concentration node are then exported into SCAPS-1D software to systematically optimize electron transport layer (ETL) thickness boundaries, establishing a complete analytical pipeline from biogenic synthesis chemistry to macroscopic thin-film solar cell efficiency.

1.3. Objectives of the Study

1.3.1. General Objective

The general objective of this study is to evaluate how varying concentration ratios of *Ocimum lamiifolium* leaf extract influence the biogenic synthesis, structural properties, and optoelectronic characteristics of zinc oxide nanoparticles (ZnO NPs), and to theoretically model their size distribution and device-level application as an electron transport layer (ETL) in perovskite solar cells (PSCs).

1.3.2. Specific Objectives

- To develop a kinetic Monte Carlo model to predict and validate nanoparticle size distributions and choose synthesis parameters.
- To synthesize ZnO nanoparticles (ZnO NPs) using *Ocimum lamiifolium* leaf extract under different extract-to-precursor concentration ratios.
- To perform phytochemical screening of *Ocimum lamiifolium* leaf extract and characterize the synthesized ZnO nanoparticles using UV–Vis, FT-IR, XRD, SEM-EDX, and TGA techniques.
- To optimize ZnO-based solar cell performance using SCAPS-1D simulation by evaluating the effects of electron transport layer (ETL) parameters on device efficiency.

1.4. Significance of the Study

This investigation provides major advancements at the intersection of sustainable nanomaterial fabrication, predictive computational physics, and next-generation photovoltaic engineering. By utilizing *Ocimum lamiifolium* (Damakesse) as a biogenic reducing and capping agent, this work establishes an eco-friendly manufacturing pathway that eliminates the hazardous organic solvents, toxic secondary effluents, and high energy demands characteristic of conventional physical and chemical synthesis protocols [39]. Consequently, this research advances the practical deployment of clean nanotechnology while preserving the precise optoelectronic parameters required for high-performance device integration.

The core scientific significance of this work lies in its systematic unraveling of concentration-dependent surface thermodynamics. Mapping the non-linear relationship between phytochemical concentration nodes and the resulting ZnO parameters provides vital insights into the competitive kinetics of biogenic nucleation, Ostwald ripening, and steric agglomeration [37]. To overcome the structural polydispersity and unpredictability traditionally inherent to green chemistry, this research introduces a stochastic Kinetic Monte Carlo (kMC) simulation model to forecast and validate atomistic size distributions. This framework offers a highly generalizable computational tool for predictive structural design, shifting biogenic nanomaterial fabrication from an empirical trial-and-error approach to a deterministic science.

From a device-engineering perspective, this study directly bridges raw botanical chemistry with the macroscopic optimization of planar heterojunction perovskite solar cells (PSCs). Integrating multi-model validated experimental data (combining structural XRD and optical EMM parameters) into SCAPS-1D simulation software provides a rigorous mechanism for identifying ideal electron transport layer (ETL) thickness boundaries. This multi-scale analytical pipeline demonstrates precisely how biogenically synthesized ZnO thin films can minimize internal series resistance, optimize band alignment, and suppress non-radiative interfacial charge recombination. Ultimately, this work proves that abundant, indigenous local flora can successfully replace synthetic, cost-intensive alternatives in high-efficiency, commercial-grade green solar technologies.

1.5. Scope of the Study

The scope of this study is bounded by the green synthesis, structural optimization, and multi-scale computational modeling of zinc oxide nanoparticles (ZnO NPs) derived from the leaf extract of *Ocimum lamiifolium* (Damakesse). Experimentally, the research is restricted to evaluating the influence of five specific extract-to-precursor volumetric concentration ratios (1:2, 1.5:2, 2:2, 2.5:2, and 3:2) on the resulting material kinetics, lattice grain boundaries, and optoelectronic properties. Material characterization is strictly confined to investigating phase purity, crystalline core size, chemical bonds, and thermal stability utilizing Ultraviolet-Visible (UV–Vis) spectrophotometry, Fourier-Transform Infrared (FTIR) spectroscopy, X-ray Diffraction (XRD), Energy Dispersive X-ray (EDX) spectroscopy, and Thermogravimetric Analysis (TGA).

Computationally, the scope encompasses a dual-layered simulation framework designed to bridge biogenic chemical processing with device-level photovoltaic performance. At the atomistic scale, a stochastic Kinetic Monte Carlo (kMC) simulation model is developed to theoretically map and predict nanoparticle size distributions based on synthesis concentration metrics, validating these digital growth profiles directly against empirical structural (XRD) and optical Effective Mass Model (EMM) boundaries. At the device scale, physical parameters from the optimized ZnO NP is exported into SCAPS-1D software to evaluate its operational performance as an Electron Transport Layer (ETL) within a planar heterojunction perovskite solar cell (PSC). This macro-level numerical simulation is restricted to optimizing ETL film thickness boundaries (20nm to 90nm) and analyzing the direct impact on macroscopic photovoltaic parameters, specifically open-circuit voltage (Voc), short-circuit current density (Jsc), fill factor (FF), and overall power conversion efficiency (PCE), utilizing a standardized FTO/ZnO/$CH_3NH_3PbI_3$/Spiro-OMeTAD/Ag device architecture.

1.6. Limitations of the Study

While this research achieves its primary objectives, a few equipment and environmental constraints defined the final scope of the investigation. The primary material limitation was the lack of access to high-resolution transmission imaging and specialized surface profiling facilities during the research period. Consequently, while three-dimensional surface morphology was verified via Scanning Electron Microscopy (SEM) and elemental purity was mapped via Energy-Dispersive X-ray Spectroscopy (EDX), the study does not provide direct internal lattice visualization through Transmission Electron Microscopy (TEM). Furthermore, this thesis does not utilize Atomic Force Microscopy (AFM) equipment, meaning that nanoscopic surface roughness parameters and localized mechanical topology profiles were not directly measured.

In addition, the transition from biogenic material synthesis to device application was conducted through a computational framework rather than physical device assembly. Due to the unavailability of high-vacuum deposition systems and the controlled, moisture-free cleanroom environments required for perovskite fabrication, the performance of the green-synthesized ZnO nanoparticles in solar cells was evaluated strictly via SCAPS-1D numerical simulation. Therefore, while the theoretical device results provide a robust optimization baseline based on physical parameters, they do not account for real-world experimental variables such as ambient humidity during thin-film casting, structural pinhole formation across the layer interfaces, or the long-term material degradation of the physical device under continuous operational illumination.

2. Literature Review

2.1. Nanomaterials

Nanomaterials are materials with at least one dimension (length, width, thickness), or a core or surface structure, measured in the nanoscale range, roughly 1 to 100 nanometers [41]. At such a microscopic scale, materials often exhibit physical, chemical, and biological properties unlike their bulk forms. Modern research emphasizes that the shift from bulk to nanoscale is not just a question of size reduction but is fundamentally driven by quantum confinement and a substantial increase in surface area relative to volume [5]. As the size of particles decreases, more of their atoms are located on the surface rather than the interior of the particle. That high surface-to-volume ratio accounts for the increased reactivity and special properties of nanomaterials, given that the atoms on the surface have higher energy and more active sites for chemical interaction[6].

Nanoparticles are a singular class of nanomaterials-zero-dimensional 0D structures in which each dimension falls in the nanoscale [1]. They represent the basic building block of nanotechnology, with highly tunable properties that can easily be modified by changing their size, shape, and surface chemistry. Contrary to bulk materials, nanoparticles are controlled by the size effect: when decreasing their diameter, all their physical and chemical properties change [42]. Chemically, due to their massive number of active surface sites, they represent one of the best catalysts for green chemistry; very useful in the chemical decomposition of persistent organic pollutants and in accelerating complex industrial reactions [18].

On the optical side, many metallic and semiconductor nanoparticles exhibit unique behaviors such as Surface Plasmon Resonance, in which light interacts with surface electrons to yield very specific modes of absorption and scattering. These are highly sensitive to the particle's local environment [43]. Quantum size effects also influence the electronic properties: energy levels become discrete at nanometer scales and change electrical conductivity and bandgap energy significantly [44]. In green synthesis, current research places an emphasis on the fact that it is a suite of phytochemicals which biological agents, such as plant extracts, carry and which act as natural ligands. These ligands stabilize high-energy nanoparticle surfaces against clumping and

preserve nanoscale properties that are critical for uses in medicine, electronics, and environmental cleanup [45].

2.1.1. Types and Classification of Nanomaterials

The classification of nanomaterials is of critical importance for the elucidation of their chemical properties. Today, nanomaterials can be classified based on two major criteria: chemical composition and physical dimension.

A. Classification Based on Composition:

Based on their chemical properties, nanomaterials can be classified into organic, inorganic, and carbon-based nanomaterials, which have unique structural properties.

1) **Organic Nanomaterials:** These nanomaterials consist mainly of organic compounds. Organic nanomaterials are often synthesized using the process of molecular self-assembly. This process utilizes weak non-covalent interactions, such as van der Waals forces, hydrogen bonding, and hydrophobic interactions, to assemble molecules into a stable structure [5]. Some examples of organic nanomaterials include dendrimers, micelles, and liposomes. These nanomaterials have been widely used in the pharmaceutical industry due to their high efficacy and biocompatibility [46].
2) **Inorganic Nanomaterials:** These nanomaterials consist of metal nanoparticles, such as gold nanoparticles, silver nanoparticles, zinc oxide nanoparticles, and titanium oxide nanoparticles. These nanomaterials have been widely used for various medical applications due to their high stability [1]. Moreover, these nanomaterials can be easily functionalized to target specific markers or pathogens [18].
3) **Carbon-Based Nanomaterials:** This type of nanomaterial is often regarded as a separate class of nanomaterials. Carbon-based nanomaterials consist mainly of carbon atoms. Some examples of carbon-based nanomaterials include C60, carbon nanotubes, and carbon nanofibers [6]. These nanomaterials have been widely used for the development of sensors and composites [43].

B. Classification Based on Dimension:

In addition to chemical composition, nanomaterials can also be classified according to the dimensionality of their morphology. This method, which was first proposed by Gleiter and then further developed, classifies nanomaterials according to the number of spatial dimensions that extend beyond the nanoscale (1-100 nm) [40].

1) **Zero Dimensional (0D):** In zero-dimensional materials, all spatial dimensions are found entirely in the nanoscale. These materials tend to form discrete particles, including spheres and aggregates, such as quantum dots and highly dispersed nanoparticles [44].
2) **One Dimensional (1D):** In one-dimensional materials, two spatial dimensions are found entirely in the nanoscale, while the third dimension is found entirely outside the nanoscale. These materials include nanorods, nanowires, and nanotubes, which can serve as efficient electron transport pathways [46].
3) **Two Dimensional (2D):** In two-dimensional materials, only one spatial dimension is found entirely in the nanoscale, typically in the form of nanometric thickness. These materials have exceptionally high surface areas and can be useful in coatings and catalytic applications [37].
4) **Three Dimensional (3D):** In three-dimensional materials, no spatial dimension is found entirely in the nanoscale. These materials consist of nanostructured components, including bundles of nanowires and nanocrystalline bulk materials [45].

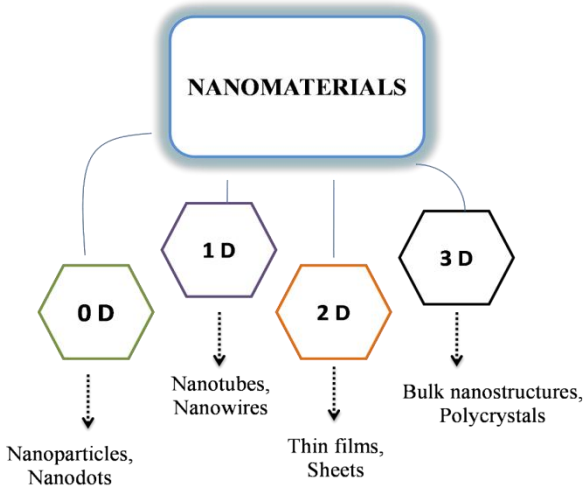

Figure 1. Classification of nanomaterials on the basis of dimensions [1].

2.2. Nanoparticles

Nanoparticles are the basic threads that bind bulk material with the intricate world of atoms and molecules. Although nanoparticle science itself accelerated following Richard Feynman's 1959 lecture, "There's Plenty of Room at the Bottom," nanoparticles themselves are nothing new, as gold and silver nanoparticles have appeared in ancient artifacts such as the Lycurgus Cup. Medieval stained glass also bears witness to the early use of nanoparticles [5]. Describing nanoparticles, we have begun with the "size effect." The percentage of atoms on the surface of a nanoparticle, as opposed to bulk materials, results in enhanced surface activity [33]. This in turn explains nanoparticles' incredible physical, magnetic, as well as special optical, properties, such as surface plasmons, which do not occur in bulk materials [1]. Nanoparticles thus play a significant role in numerous areas, from medicine, in which nanoparticles can be used as drug carriers, through green chemistry, where they can be used as pollution rectifiers.

2.3. Metal Oxide Nanoparticles

Metal oxide nanoparticles represent a major family of inorganic materials for which researchers value outstanding stability and versatile functionality. They are formed by the reaction of transition metals with oxygen, resulting in structures whose electronic behavior spans from metallic to insulating [41]. These transition metal oxides are particularly valued for their semiconductor properties, the bandgap energies of which can be adjusted through changes in either particle size or shape [18]. Unlike pure metal nanoparticles, which may quickly oxidize in air, metal oxides are usually more chemically stable, with higher melting points, and are therefore better suited to demanding industrial conditions [43].

Among the transition metal oxides, ZnO is at the forefront of green synthesis studies. Its popularity owes to the rare combination of a large direct bandgap of 3.37 eV and an exciton binding energy of 60 meV at room temperature, which drives intense effort toward its use in optoelectronic and catalytic applications [40]. Besides, ZnO has been classified as Generally Recognized as Safe (GRAS) by the FDA, which means that this material can be considered much more biocompatible than other oxides, such as Titanium Dioxide or Copper Oxide [6]. The minimal toxicity, together with high antimicrobial action and easily prepared by plant extracts

like Ocimum lamifolium, sustains its central position in green nanotechnology efforts directed to medical and environmental safety [44].

2.4. Synthesis of Nanoparticles

The synthesis of nanoparticles is traditionally divided into two main strategic categories: Top-Down and Bottom-Up. In the top-down method, a bulk material is broken down into nanoscale components using techniques such as milling, etching, and ablation [6]. Although the method is successful in producing large quantities of nanoparticles, it is often associated with surface imperfections and high energy costs. The bottom-up method, also called the self-assembling method, on the other hand, is the assembly of atoms or molecules to form a material using chemical reactions and physical deposition [5]. The bottom-up method is widely used today because of the high degree of control over the size, shape, and structure of the nanoparticles.

The methods of synthesizing nanoparticles have been classified according to the nature of the synthesis process itself: physical, chemical, and biological. Although the traditional physical and chemical methods have been successful and allow for high degrees of accuracy, they often require sophisticated equipment and high pressure, or the use of environmentally hazardous reagents such as reducing agents, which have adverse health and environmental impacts [1]. As such, recent research efforts have been devoted to the development of a more environmentally friendly method of synthesis, often called the “biological” or “green” method. The green method uses biological systems such as plants, bacteria, and fungi to synthesize nanoparticles [43]. The green method is recognized to be environmentally friendly and is used to synthesize nanoparticles that can be used for a variety of applications, including medicine and the environment [44].

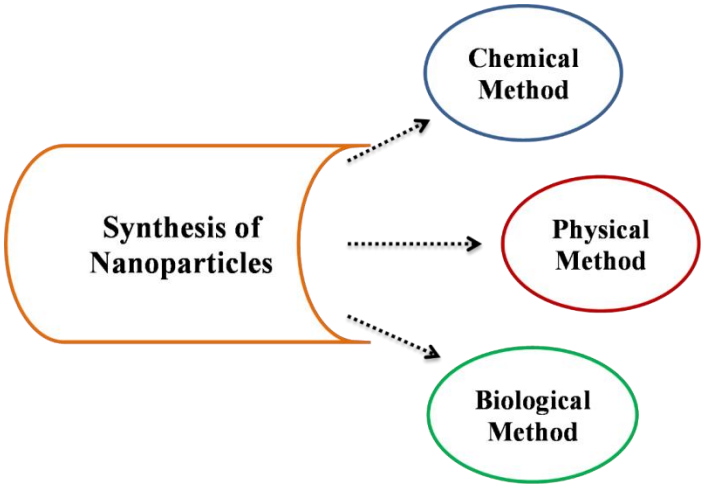

Figure 2. Different routes for the synthesis of nanoparticles [28].

2.4.1. Chemical Methods

Chemical methods are widely employed to synthesize nanoparticles because the process results in high yield and allows size and shape control. They involve the reaction of two chemical precursors dissolved in a liquid to form particles.

2.4.1(a). Sol-Gel Method:

The Sol-gel method is a versatile and mainly wet chemical method for the synthesis of metal oxide particles. It involves the process of changing from a colloidal liquid phase, called a sol, to a solid, called a gel[6]. A metal alkoxide or salt hydrolyzes and undergoes condensation to form the gel. Drying and then calcination always follow. This produces highly crystalline metal oxide nanoparticles[5].

2.4.1(b). Microemulsion method:

The microemulsion method, which is also known as the micelle method or reverse micelle method, uses surfactants to create a dispersion of two immiscible liquids. In this method, water droplets retained in an oil medium using surfactants are used as nanoscale reactors[1]. The addition of precursors to these water droplets restricts the reaction volume to the nanoscale, thus limiting the growth of nanoparticles. The nanoparticles obtained by this method have precise dimensions and shapes, although they also have large surfactant-usage requirements[18].

2.4.2. Physical Methods

Physical methods use mechanical or thermal energy to fragment a material into nanoparticles, following a top-down approach. Unlike chemical synthesis, the importance of physical synthesis lies in the production of ultra-pure nanoparticles in the absence of any surfactant or reagent, which could contaminate the final product [5].

A. Ball Milling

Ball milling is a mechanical technique involving the high-energy grinding of a material. The material is ground in a rotating vessel containing grinding balls, usually made of steel or zirconia. The kinetic energy of the grinding balls and the material causes the material to deform and fragment into nanoparticles [6].The technique is very suitable for the production of nanoparticles at a large scale but is often associated with the introduction of structural defects and contaminants during the process [1].

B. Laser Ablation

Laser ablation is a technique involving the removal of material from a solid target using a strong laser beam. The laser ablation technique is usually performed in a liquid medium, known as Laser Ablation in Liquids (LAL). The laser beam is focused onto the material, causing rapid heating and vaporization of the material. The vaporized material then forms a plasma plume, and nanoparticles are formed when the material condenses in the liquid medium [18]. The technique is very precise and is also called a “physical-green” technique, as it is performed without the use of any reagent or surfactant, thus yielding ultra-pure nanoparticles, especially for biological and electronic applications where the presence of contaminants is undesirable[47].

2.4.3 Biological Methods (Green Synthesis)

The biological methods, also known as Green Synthesis, are a green, bottom-up, and cost-effective alternative to conventional methods. This method utilizes the inherent properties of biological materials, such as bacteria, fungi, and plant extracts, to act as both reducing and stabilizing agents for metal ions [43]. Microorganisms can reduce metal ions to nanoparticles either intracellularly (inside the cells) or extracellularly (outside the cells) with the help of specific enzymes like nitrate reductases, with fungi-based methods reported to show high yields

of nanoparticles in spherical or triangular shapes [48]. Meanwhile, the use of plant extracts for synthesizing nanoparticles has been found to be the most popular green method due to the wide availability of plant materials, especially *Ocimum lamifolium*. Plants contain bioactive compounds like polyphenolic, flavonoid, and terpenoid groups, which enable the rapid reduction of metal salts to nanoparticles at room temperature in a one-step reaction [40].

The major advantages of green synthesis span non-toxicity, cost-effectiveness, and sustainability. First, this method ensures non-toxicity by avoiding the use of harmful reagents like sodium borohydride and hydrazine, making the nanoparticles produced in this method biocompatible for use in medical fields [44]. Additionally, it offers cost-effectiveness by utilizing renewable resources like agricultural waste, which helps in reducing the cost of the starting material [46]. Finally, it promotes long-term sustainability because the entire process is carried out under normal conditions of temperature and pressure, which helps in reducing the energy and waste generated in the process, as described in the 12 green chemistry principles [45].

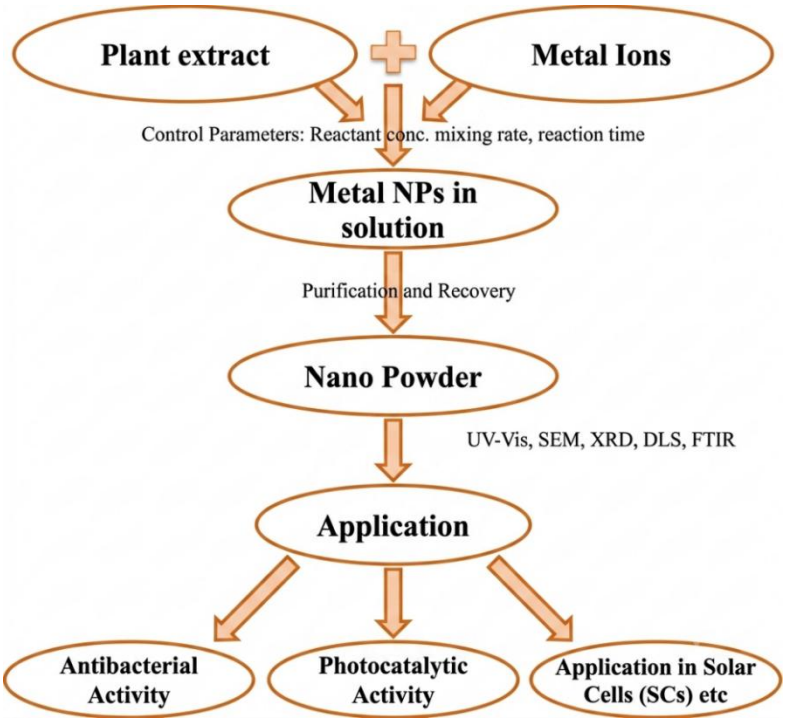

Figure 3. Flowchart for the biosynthesis of nanoparticles

2.5. Ocimum Lamifolium (Damakesse)

Ocimum lamifolium, also referred to as "Damakesse" in Ethiopia, is an important medicinal shrub belonging to the Lamiaceae family. This medicinal plant has gained much recognition in traditional Ethiopian medicine and has also emerged as an important tool in the green synthesis of nanoparticles in the context of nanotechnology.

2.5.1. Botanical Description and Distribution

Ocimum lamifolium is an indigenous sub-shrub/shrub found in the region between an altitude of 1,200 to 3,000 meters above sea level [44]. This medicinal plant is characterized by its woody stem, opposite oval-shaped leaves with serrate or crenate margins, and the distinct pungent odor of the leaves on being crushed. In Ethiopia, O. lamifolium is found in its natural habitat in areas such as forests and clearings but is mostly grown in home gardens due to its use as the first line of treatment for cough, fever, and skin infections [49]. This plant has an extensive distribution in the highlands of Ethiopia and has an ability to grow profusely, making it easily available and accessible for use in green synthesis[50].

2.5.2. Phytochemical Composition

The leaves of O. lamifolium contain a complex mixture of secondary metabolites, which play an important role in the green synthesis process. The most important compounds identified in the leaves of O. lamifolium are polyphenols, flavonoids, tannins, and terpenoids [40]. These phytochemical compounds contain important functional groups such as hydroxyl (-OH) and carbonyl (-C=O). These two functional groups play an important role in the green synthesis process. These phytochemical compounds perform two important roles in the green synthesis process:

1. Reducing Agents: These compounds donate electrons to the metal precursor (Zn^{2+}), which in turn helps in the reduction of the metal into stable metal oxide nuclei[51].

2. Capping and Stabilizing Agents: These compounds, particularly flavonoids and terpenoids, adsorb on the surface of the formed nanoparticles, thus forming a protective layer on the surface of the nanoparticles. This layer prevents the nanoparticles from agglomerating and also helps in controlling the size of the nanoparticles[18].

Figure 4. Leaves of plant,Ocimum lamifolium (Damakesse)

2.6. Zinc Oxide Nanoparticles (ZnO NPs)

Zinc oxide (ZnO) is a widely used n-type semiconductor material that is considered to be one of the most important components of nanotechnology because of its exceptional physical, chemical, and biological characteristics. Zinc oxide is a semiconductor material with a large direct bandgap of 3.37 eV and a high exciton binding energy of 60 meV, allowing it to exhibit excitonic emission at room temperature[52]. In contrast to other metal-based nanoparticles, ZnO is chemically stable and has excellent electrochemical coupling and a wide range of absorption from ultraviolet to infrared light. In addition, ZnO is considered a highly biocompatible compound and is classified by the U.S. Food and Drug Administration (FDA) as Generally Recognized as Safe (GRAS)[18]. In terms of green nanotechnology, ZnO NPs have been widely used because of their synthesis using plant-based extracts such as Ocimum lamifolium, which is considered a safe and environmentally friendly alternative to the use of dangerous chemical reagents[40].

2.6.1. Structure of ZnO

The crystal structure of zinc oxide is usually one of three allotropes: hexagonal wurtzite, cubic zinc blende, and cubic rocksalt. At room temperature, the most thermodynamically stable allotrope is the hexagonal wurtzite structure, which is the one most commonly synthesized using green synthesis techniques with plant extracts like Ocimum lamifolium [53]. The structure of the

wurtzite allotrope consists of two hexagonal close-packed lattices, meaning that the lattice is composed of alternating zinc and oxygen ions. Each zinc ion is tetrahedrally coordinated with four oxygen ions, and vice versa. A notable property of this structure is its non-centrosymmetric symmetry, meaning it does not have a center of inversion. This property is what contributes to the piezoelectricity and spontaneous polarization of the crystal, making it useful for sensor devices and energy harvesting nanogenerators [54].

2.6.2. Properties of ZnO Nanoparticles

The wide range of applications of ZnO nanoparticles, from industrial to environmental to medical, can be largely accounted for by their unique physical and chemical properties.

A. Physical Properties

The most important physical property of ZnO nanoparticles is their large surface area to volume ratio. As the particle diameter approaches the nanoscale, the ratio of atoms on the surface to those in the bulk increases, thus providing greater surface energy and hence higher catalytic activity. Additionally, ZnO has high thermal stability, with a melting point of 1975°C. This means that the nanoparticles retain their structure at high temperatures, which is often required for many industrial applications [55].

B. Mechanical Properties

ZnO nanoparticles possess high hardness and a large modulus of elasticity. The most important mechanical property of ZnO nanoparticles, however, is their piezoelectricity, which is a result of their noncentrosymmetric wurtzite crystal structure. When subjected to stress, the position of the cations and the anions changes, thus generating a dipole moment. This, in turn, produces an external electric field. Thus, ZnO nanostructures, such as nanowires, can be used to generate electrical energy from ambient vibrations, such as wind, human movement, or sound[34].

C. Photoluminescence Properties

The optical properties of ZnO nanoparticles (NPs) are characterized by the dual-emission phenomenon. These NPs emit sharp near-band-edge (NBE) emission in the ultraviolet region, corresponding to the recombination of free excitons. Simultaneously, ZnO NPs also emit broad

deep-level emission in the visible region, corresponding to defects such as oxygen vacancies or zinc interstitials. Hence, ZnO NPs are essential for optical sensor devices, LEDs, and as an active component in sunscreens, which absorb and scatter harmful UV-A and UV-B rays of the sun's spectrum [18].

D. Electrochemical Properties

ZnO NPs have high isoelectric points, approximately 9.5, and demonstrate excellent biocompatibility. These NPs facilitate fast kinetics in the transfer of electrons between the bio-analyte and the surface of the electrode. This phenomenon is heavily employed in the construction of highly sensitive bio-sensors. For example, in glucose bio-sensors, the high surface energy of ZnO NPs helps to immobilize enzymes on the surface of the sensor, leading to faster kinetics and lower detection limits in clinical diagnostics [52].

E. Electrical Properties

ZnO NPs are characterized by their large band gap energy, approximately 3.37 eV, making them transparent in the visible region and highly active in the ultraviolet region. Additionally, ZnO NPs have an exceptionally high exciton binding energy of 60 meV, which is the most important electrical characteristic. This energy value is much higher than the thermal energy available at room temperature, kBT ≈ 26 meV, making ZnO NPs stable under room conditions. This stability allows optoelectronic devices such as ultraviolet lasers and solar cells to function optimally without requiring cryogenic cooling [45].

2.6.3. Green Synthesis of Zinc Oxide Nanoparticles Using Plant Extracts

The green approach for the synthesis of ZnO NPs is a biogenic, bottom-up approach, utilizing the secondary metabolites of "Ocimum Lamifolium" as green alternatives for the conventional chemical reagents used for nanoparticle synthesis. This approach is generally preferred over other chemical approaches, as it avoids the use of toxic reagents such as sodium borohydride or hydrazine. The green approach for the synthesis of ZnO NPs begins with the preparation of a water extract of "O. lamifolium", which is known for its high content of bioactive molecules, such as flavonoids, polyphenolic, and terpenoid compounds. When mixed with a zinc precursor, such as zinc acetate dihydrate [Zn(CH3COO)2·2H2O], the hydroxyl (-OH) and carbonyl (C=O)

functional groups of the phytochemicals act as ligands, binding to the zinc ions, resulting in a stable complex [40]. When the mixture is heated at a temperature ranging from 60 to 80°C, the complexes decompose, resulting in zinc hydroxide [Zn(OH)2] clusters, which act as a template for the formation of ZnO NPs. The final step is the collection of the precipitate, which is then subjected to a thermal treatment at a temperature ranging from 300 to 500°C, resulting in a highly stable crystalline structure of ZnO NPs. During this reaction, the phytochemicals adsorb onto the surface of the NPs, acting as capping agents, which prevent uncontrolled growth of the NPs [44].

2.6.4. Effect of Synthesis Parameters

A. Effect of Extract Concentration

The proportion of O. lamifolium extract and zinc salt precursors is a critical factor for determining the final shape of the particles. A strategic increase in the concentration of the plant extract will provide a higher number of capping agents, which will limit the crystal plane growth, resulting in a smaller final product size and higher monodispersity [18]. However, it is important to note that a threshold limit is required, as a high concentration of plant extract may increase the rate of nucleation, resulting in agglomerated particles or irregular shapes [56].

B. Effect of pH and Temperature

1. PH: The pH value of the reaction medium is a critical factor for determining the final shape of the particles. The pH value will influence the ionization state of the phytochemicals. At a higher pH value (8-11), the deprotonation of phenolic rings is favored, resulting in a higher reductive potential, which is favorable for the formation of smaller, more stable particles. At a lower pH value, the formation of larger, rod-like, or fragmented particles is common [57].

2. Temperature: The temperature of the reaction medium is a critical factor for determining the final shape of the particles. A moderate increase in temperature will increase the rate of reduction, allowing the system to overcome the activation energy barrier for nucleation. Higher temperatures are required for the formation of pure hexagonal phases of zinc oxide, allowing for the easy removal of organic impurities from the crystal lattice [52].

2.6.5. Optical Modeling of ZnO Nanoparticles: Mie Theory Framework

In order to comprehend the function of ZnO nanoparticles in the manipulation of light in the PSC device, it is essential to have an in-depth understanding of the optical interactions of ZnO nanoparticles. ZnO is a semiconductor material with a bandgap of approximately 3.37 eV. It has a high refractive index in the visible regime of the solar spectrum. This makes it an efficient material for dielectric-type light scattering while simultaneously minimizing the absorption of solar radiation. The optical response of ZnO nanoparticles, including the phenomena of absorption, extinction, and the enhancement of the local electric field, is highly size- and aspect-ratio-dependent[58,59].

Mie theory provides an exact analytical solution to Maxwell's equations for scattering and absorption of electromagnetic waves by spherical particles [58]. For ZnO nanoparticles embedded in a perovskite or transport layer,the extinction(Q_{ext}),scattering (Q_{sca}), and absorption (Q_{abs})cross-sections are expressed as:

$$Q_{\text{ext}}=\frac{2\pi}{k^2}\sum_{n=1}^{\infty}(2n+1)\,\text{Re}(a_n+b_n) \quad (1)$$

$$Q_{\text{sca}}=\frac{2\pi}{k^2}\sum_{n=1}^{\infty}(2n+1)(|a_n|^2+|b_n|^2) \quad (2)$$

$$Q_{\text{abs}}=Q_{\text{ext}}-Q_{\text{sca}} \quad (3)$$

where $k=2\pi/\lambda$, a_n and b_n are Mie coefficients determined by particle radius r, wavelength λ, and the complex refractive index of ZnO relative to the surrounding medium.

The theory assumes the particles are embedded in a homogeneous medium (the perovskite layer with refractive index $n \approx 1.5$. When the particle radius r is much smaller than the wavelength ($r \ll \lambda$), Mie theory simplifies to Rayleigh scattering. The scattering cross-section in this regime is given by [58]:

$$Q_{\text{sca}} = \frac{128\pi^5 r^6}{3\lambda^4}\left|\frac{m^2-1}{m^2+2}\right|^2 \quad (4)$$

where m is the relative refractive index (n_{ZnO} / n_{perov}). This formula demonstrates that scattering intensity scales with r^6, making particle size a dominant factor in optical path length enhancement.

The optical properties of zinc oxide (ZnO) nanoparticles are heavily dictated by size. In the Rayleigh scattering regime ($r << \lambda$), scattering efficiency scales as r^6 while absorption scales as r^3 [58], meaning small nanoparticles (< 20 nm) exhibit weak far-field scattering but can provide localized near-field enhancement. Intermediate sizes (50-150 nm) transition into the Mie scattering regime, significantly enhancing forward dielectric scattering to improve light trapping within the perovskite absorber. However, excessively large particles increase surface roughness and induce parasitic optical losses. Because ZnO is a dielectric material rather than a plasmonic metal, these effects stem from high-index Mie resonances rather than free-electron oscillations, making precise size optimization vital for broadband light-harvesting [59,60].

2.6.6. Applications of ZnO Nanoparticles

A. Antibacterial Activity

ZnO nanoparticles display strong antimicrobial activity against a wide spectrum of pathogens, including Gram-negative bacteria Escherichia coli and Gram-positive bacteria Staphylococcus aureus. The antimicrobial action of ZnO nanoparticles is complex and can be explained by the following aspects:

1. **Generation of Reactive Oxygen Species (ROS):** Under ambient light, ZnO nanoparticles catalyze the production of superoxide radicals (•O2−) and H2O2, causing significant oxidative damage to the bacterial cell membrane [53].
2. **Disrupting the Cell Membrane:** The nanoparticles accumulate at the bacterial envelope and cause structural damage, resulting in the leakage of intracellular components.
3. **Release of Zn2+ Ions:** The slow release of Zn2+ ions from the nanoparticles interferes with the normal functioning of bacterial enzymes[45].

B. Photocatalytic Activity

ZnO nanoparticles are effective photocatalysts in the remediation of pollutants from the environment, especially the decomposition of synthetic dyes such as methylene blue. Upon absorption of photons of energy equal to or greater than the bandgap of the material (Eg ≈ 3.3eV), the valence band electrons are excited to the conduction band, leaving holes in the valence band. The holes react with H2O molecules, producing •OH radicals, whereas the excited electrons react with dissolved O2 molecules, yielding •O2− radicals [55]. The reactive radicals attack the chromophores of the organic dyes and lead to the decomposition of the dyes into mineralized products such as CO2 and H2O [59].

C. Application in Perovskite Solar Cells (PSCs)

In the context of photovoltaics (PV), Zinc Oxide (ZnO) nanoparticles are used as a superior alternative to Titanium Dioxide (TiO_2) due to their unique optoelectronic properties.

When integrated as an Electron Transport Layer (ETL), ZnO acts as a high-mobility n-type semiconductor with a bulk mobility in the range of 205-300 $cm^2V^{-1}s^{-1}$. This exceptional mobility allows for efficient electron extraction from the perovskite active layer, which drastically reduces charge accumulation at the interface, minimizes non-radiative recombination, and ultimately improves the short-circuit current density (Jsc) [60]. Furthermore,ZnO offers the distinct advantage of low-temperature processing. Unlike TiO_2, which requires a demanding high-temperature sintering step at 500°C, ZnO nanoparticle layers can be successfully processed at temperatures below 150°C. This low thermal budget is a strict requirement for the fabrication of flexible optoelectronic devices on plastic substrates like polyethylene terephthalate (PET) [61].

The material also exhibits highly favorable energy level alignment; the ZnO conduction band minimum, centered at -4.2eV, aligns precisely with the conduction band level of standard lead halide perovskites, ensuring a negligible energy barrier for smooth, efficient electron injection [60]. Finally, ZnO contributes to UV shielding and device stability. Even though it possesses inherent photocatalytic activity, when it is utilized as a front contact, the nanoparticle layer functions as an effective UV filter. This filtering action protects the vulnerable organic cations within the perovskite absorber layer from high-energy UV irradiation, thereby mitigating photochemical degradation and potentially expanding the overall operational lifetime of the solar cell [62].

2.7. Perovskite Solar Cells

2.7.1. Structure and Working Principle

Perovskite solar cells (PSCs) have been recognized as one of the most promising photovoltaic technologies owing to their superior power conversion efficiency, low-cost fabrication process, and flexibility in adjusting their optoelectronic properties[60]. The general structure of a PSC consists of a transparent conducting oxide (TCO) substrate, an electron transport layer (ETL), a perovskite absorber layer, a hole transport layer (HTL), and a metal back contact. The TCO layer, which is composed of indium tin oxide (ITO) or fluorine-doped tin oxide (FTO), serves as the anode and allows light to enter the solar cell. The ETL layer, which is constructed from TiO2 or ZnO, selectively extracts and transports electrons from the perovskite layer while hindering the transport of holes. On the other hand, the HTL layer, which is formed from spiro-MeOTAD or PEDOT:PSS, assists the transport of holes to the cathode and blocks the recombination of electrons[61,62]. The perovskite layer, which is composed of an organometallic halide perovskite such as CH3NH3PbI3, exhibits strong light-harvesting capability owing to its strong absorption coefficient and long carrier diffusion length[63].

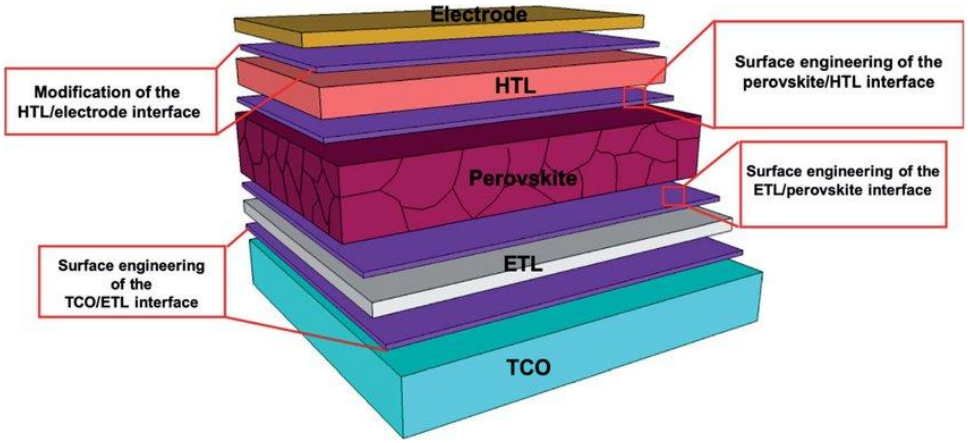

Figure 5: Typical perovskite solar cell architecture[61].

Upon illumination, the perovskite layer absorbs light to create electron-hole pairs, also referred to as excitons. However, these pairs are then quickly separated at the interfaces by the ETL and HTL layers. The electrons are injected into the ETL layer and then moved toward the anode, whereas the holes are injected into the HTL layer and moved toward the cathode. This separation

of the generated pairs reduces the recombination effect, thus increasing the generation of photocurrent [64]. However, the efficiency of the process is determined by the inherent properties of the perovskite material as well as the quality of the layers [65].

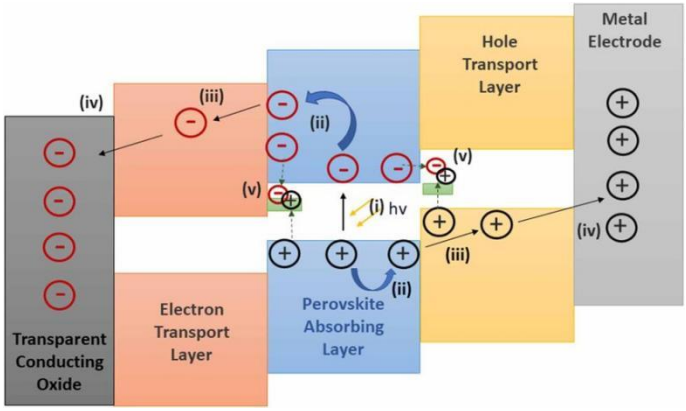

Figure 6. Schematic diagram of the light-to-electricity conversion mechanism in a typical n-i-p perovskite solar cell. The mechanism includes: (i) light absorption and charge generation; (ii) exciton dissociation and charge transport; (iii) charge transport to the ETL and HTL; (iv) charge collected by the TCO and metal electrode; and (v) charge recombination induced by interface trap states (indicated by a dashed green line)[64].

However, recent research has shown that the addition of nanoparticles, such as ZnO nanoparticles, to the perovskite layer can lead to further improvements in the absorption of light and the efficiency of the device. The nanoparticles act to scatter the light, effectively increasing the path length of the light within the active layer. In addition, the near-field effects of the nanoparticles can increase the intensity of the light, resulting in an increase in the excitons generated in the device. The nanoparticles' size, shape, and concentration are important parameters that can influence the far-field scattering, near-field enhancement, and finally the photocurrent generated [66,67]. Therefore, the nanoparticles' shape and concentration can have a considerable impact on the light management and the efficiency of the perovskite solar cells.

2.7.2. Optical Loss Mechanisms in Perovskite Solar Cells

Optical losses in perovskite solar cells (PSCs) significantly limit device efficiency by reducing the fraction of incident light absorbed by the active perovskite layer. The main loss mechanisms include:

1. Reflection Losses:

A portion of the incident light is reflected at the air/glass and interface layers due to refractive index mismatch. This reflection reduces the number of photons entering the perovskite absorber. Anti-reflective coatings or scattering layers (e.g., ZnO nanoparticles) can mitigate this effect by increasing light coupling [53,54].

2. Parasitic Absorption:

Light absorption by non-active layers, such as the electron transport layer (ETL), hole transport layer (HTL), or transparent conductive oxide (TCO) electrodes, does not contribute to photocurrent generation. Incorporating scattering ZnO nanoparticles can redirect light away from these layers and into the perovskite layer, reducing parasitic losses [55].

3. Incomplete Light Harvesting:

Even after entering the cell, photons may pass through the perovskite layer without absorption due to limited optical path length, particularly for wavelengths near the band-edge. Light-trapping strategies, such as forward and backward scattering by ZnO nanoparticles, increase the optical path and improve absorption across a broader spectrum [56].

2.7.3. Light Management Strategies

Efficient light management is critical in perovskite solar cells (PSCs) to maximize photon absorption and minimize optical losses. Various nanostructures and mechanisms have been explored to enhance light harvesting:

1. Plasmonic Nanoparticles:

Metallic nanoparticles (e.g., Au, Ag) support localized surface plasmon resonances (LSPRs) that concentrate electromagnetic fields near the particle surface. This near-field enhancement increases exciton generation in the adjacent perovskite layer, while far-field scattering redirects incident light into the absorber, improving optical path length and light absorption [54,55].

2. Dielectric Nanoparticles (Including ZnO):

High-refractive-index dielectric nanoparticles, such as ZnO, provide strong light scattering without significant parasitic absorption, unlike metallic plasmonic nanoparticles. ZnO

nanoparticles can be engineered in size, shape, and concentration to optimize both forward and backward scattering, increasing the optical path within the perovskite layer and enhancing absorption across a broad wavelength range [54,55].

3. Scattering Enhancement:

Embedding nanoparticles in the electron transport layer (ETL) or on the perovskite surface can create scattering centers that redirect unabsorbed light back into the active layer. Optimized scattering angles improve light trapping and reduce transmission losses, particularly for near-infrared photons [56].

4. Near-Field Electromagnetic Enhancement:

Localized electromagnetic fields generated around nanoparticles intensify the light intensity in their immediate vicinity. For ZnO nanoparticles, careful control of particle size and aspect ratio can maximize near-field enhancement without introducing significant recombination sites, leading to higher exciton generation rates and improved photocurrent [57].

2.8. ZnO Nanoparticles in Perovskite Solar Cells

ZnO nanoparticles play a multifaceted role in perovskite solar cells (PSCs), influencing both charge transport and light management:

1. Role as Electron Transport Material (ETM):

ZnO is widely used as an electron transport layer due to its high electron mobility, wide bandgap (~3.3 eV), and excellent energy level alignment with perovskite absorbers. Incorporating ZnO nanoparticles improves electron extraction and reduces recombination at the interface, enhancing overall device efficiency [53,54].

2. Optical Spacer and Scattering Layer:

ZnO nanoparticles can act as optical spacers between the perovskite absorber and back contact, improving light confinement. By scattering incident light into the perovskite layer, they increase the effective optical path length, allowing for enhanced photon absorption, particularly in thin-film PSCs [54,55].

3. Morphology-Dependent Light Trapping:

The shape and size of ZnO nanoparticles—spherical, rod-like, or ellipsoidal—directly influence light trapping. Nanorods or elongated nanoparticles can induce anisotropic scattering and near-field enhancement, which improves directional light coupling into the perovskite layer. Fine-tuning morphology is therefore critical for maximizing light harvesting [55,56].

4. Concentration-Dependent Photocurrent Enhancement:

The number density of ZnO nanoparticles determines collective scattering and near-field enhancement effects. At optimal concentrations, nanoparticles enhance photocurrent by increasing exciton generation and reducing reflection losses. Excessive concentrations may lead to aggregation, parasitic absorption, or recombination losses, reducing efficiency [60.61].

3. Materials and Methods

3.1. Chemicals and Materials

The fresh leaves of *Ocimum lamiifolium* were obtained from the local regions of Bahir Dar, Ethiopia, and their botanical identity was formally authenticated by a taxonomist at the local herbarium. Zinc acetate dihydrate [$Zn(CH_3COO)_2.2H_2O$, 99.9\%], utilized as the zinc precursor, along with ethyl alcohol and acetone, were used as received. All chemicals employed in this study were of analytical grade and required no further purification. All glassware was thoroughly cleaned using double-distilled water and ethanol, then dried in an oven prior to use. The equipment employed in the synthesis of nanoparticles included an electronic digital balance for precise mass measurements, Whatman No. 1 filter paper for the separation of resulting solids from the liquid phase, and a magnetic stirrer with a hot plate (IKA RH digital, Germany) to ensure a consistent mixture by agitation. A water bath maintained at a constant temperature was utilized for the extraction process, while an oven was used for drying the synthesized samples. Other essential items included volumetric flasks for the preparation of various solution concentrations, measuring cylinders for liquid volume measurements, a ceramic crucible for sample handling, and a thermometer for accurate temperature monitoring throughout the synthesis and extraction phases.

3.2. Simulation of ZnO synthesis using kinetic Monte Carlo.

Prior to experimental synthesis, a kinetic Monte Carlo (kMC) simulation was conducted to systematically investigate and identify the optimal physicochemical conditions required to yield zinc oxide (ZnO) nanoparticles with dimensions suitable for photovoltaic device fabrication. The simulation framework was implemented utilizing the open-source Python package kMCpy. The core operational parameters utilized during the stochastically driven simulation are comprehensively outlined in Table 1.

Through a systematic iterative optimization process, the simulation parameters were varied to achieve a target nanoparticle diameter of approximately 16.5nm(corresponding to an optimized final radius, r of 8.25nm). This ultra-small diameter target was selected because ZnO clusters below 20nm exhibit enhanced quantum confinement effects, significantly widening the optical

bandgap beyond the bulk value of 3.37eV [63]. In perovskite solar cells (PSCs), this structural reduction increases the optical transparency of the Electron Transport Layer (ETL), completely suppressing parasitic blue-shifted photon absorption and maximizing light transmission into the underlying perovskite absorber [64]. Furthermore, a compact packing of 16.5 nm spheres enables the low-temperature fabrication of pinhole-free, highly uniform thin films that provide direct, short pathways for rapid electron extraction before non-radiative recombination can manifest at the heterojunction interface [65]. The computationally optimized conditions derived from this model were subsequently established as the baseline for the physical experimental green synthesis of the ZnO nanoparticles.

Table 1. Parameters used in the kinetic Monte Carlo simulation of ZnO nanoparticle synthesis

Parameter	**Value**	**Unit**	**Description**
precursor	Zinc Acetate	—	Zinc source
precursor_concentration	0.1	M	Precursor molarity
solvent	Deionized Water	—	Reaction solvent
plant_extract	Ocimum Lamifolium	—	Reducing/capping agent
leaf_mass	10	g	Powdered dry leaves
extract_volume	100	mL	Extract preparation volume
pH	12	—	Adjusted using NaOH
NaOH_concentration	0.1	M	pH adjustment solution
reaction_temperature	60	°C	Synthesis temperature
reaction_time	3	h	Solution reaction duration
centrifuge_speed	4000	rpm	Separation speed
centrifuge_time	20	min	Separation duration
drying_temperature	100	°C	Oven drying
drying_time	12	h	Drying duration
calcination_temperature	400	°C	Calcination temperature
calcination_time	2	h	Calcination duration
target_radius	8.25	nm	Desired nanoparticle radius
critical_radius_r0	2	nm	Initial critical nucleus radius
diffusion_rate_constant_K	0.55	nm^3/h	Diffusion-controlled constant
surface_rate_constant_k2	4.4	nm^2/h	Surface reaction constant

The nanoparticle growth kinetics were modeled using both diffusion-controlled and surface-reaction-controlled growth mechanisms. The diffusion-controlled growth process was described by

$$r^3 = Kt + r_0^3 \quad (5)$$

while the surface-reaction-controlled growth was represented by

$$r^2 = k_2 t + r_0^2 \quad (6)$$

where r is the nanoparticle radius, r_0 is the critical nucleus radius, t is the reaction time, K is the diffusion-controlled growth constant, and k_2 is the surface-reaction-controlled rate constant

3.3. Experimental

3.3.1. Preparation of Ocimum Lamifolium Leaf Extract

To obtain the extracts, freshly collected leaves were washed repeatedly with running tap water to remove dust and debris, followed by repeated washing with distilled water to remove surface impurities. The leaves were then shade-dried at a room temperature of 25 ± 2°C for 15 days to prevent the degradation of phytochemicals, such as volatile oils and polyphenols. After drying, the leaves were powdered using a sterilized mechanical grinder and sieved to obtain uniform-sized particles to ensure efficient extraction. 10 g of the powdered leaves were placed in a 250 ml conical flask with 100 ml of double-distilled water. The mixture was then heated in a water bath at 60°C for 3hr with constant stirring to leach out the bioactive metabolites. The solution was allowed to cool to room temperature and filtered using Whatman No. 1 filter paper to remove impurities. Finally, the resulting clear filtrate was stored in a refrigerator at 4°C for further use in the synthesis reaction. The general procedure for the preparation of the plant extract is shown in Figure 7.

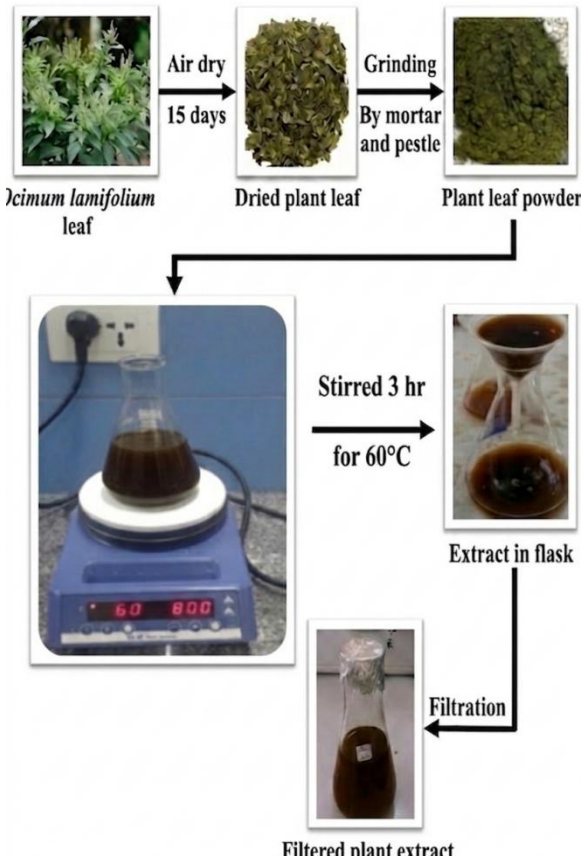

Figure 7. Steps involved in the preparation of ocimum lamiifolium leaf extract

3.4. Phytochemical Screening of *Ocimum lamiifolium* Leaf Extract

Qualitative analysis was performed to investigate the presence of key reducing, stabilizing, and capping agents in the *Ocimum lamiifolium* leaf extract. The evaluation of flavonoids involved the addition of 4 ml of the plant extract to a test tube, followed by treatment with 2 ml of a 10% NaOH solution. To test for alkaloids, 2 ml of the *Ocimum lamiifolium* extract was mixed with 5 drops of Wagner's reagent (prepared using 1.27 g of iodine and 2.0 g of potassium iodide in 100 ml of water). The glycoside examination was carried out by dissolving a small amount of the extract in 1 ml of distilled water, followed by the addition of aqueous sodium hydroxide. The tannin evaluation was conducted by mixing 1 ml of the plant extract with 1 ml of distilled water and 2–3 drops of a lead acetate [$Pb(C_2H_3O_2)_2$]solution in a test tube. Lastly, the phenol test involved adding a few drops of a 10% aqueous ferric chloride solution to 1 ml of the *Ocimum lamiifolium* extract in a test tube.

3.5. Synthesis of Zinc Oxide Nanoparticles

Biosynthesis of ZnO Nanoparticles: The synthesis of zinc oxide nanoparticles followed a biogenic chemical precipitation-calcination procedure, leveraging the high reduction potential of the *O. lamifolium* leaf extract. To optimize the synthesis, five distinct reaction sets were prepared by maintaining a constant 100 mL volume of 0.1 M Zinc Acetate precursor while systematically varying the volume of the plant extract (50 mL, 75 mL, 100 mL, 125 mL, and 150 mL). The extract was added dropwise to the precursor solution under vigorous magnetic stirring at a constant temperature of 60°C to facilitate the complexation of zinc ions with the plant phytochemicals.

During the reaction, the pH was monitored with a digital pH meter, and dilute 0.1 M NaOH was slowly added to the mixture until an alkaline range of 8–12 was attained, facilitating the formation of the zinc hydroxide intermediate. The successful reduction and complexation of zinc ions by the plant metabolites were evidenced by the appearance of a creamy or milky-white precipitate. To ensure the completion of the reaction, stirring was continued for an additional 2 hours after the final addition of the extract.

To isolate the nanoparticles, the resulting suspension was centrifuged at 4000 rpm for 20 minutes. For purification, the retained pellet underwent three wash cycles with deionized water followed by two wash cycles with ethanol, effectively removing excess precursors, salt byproducts like sodium acetate, and residual organic impurities. The purified nanoparticles were initially dried at 100°C for 12 hours before being transferred to a porcelain crucible for calcination at 400°C for 2 hours. This thermal treatment was essential for the complete conversion of the hydroxide intermediate into highly crystalline ZnO nanopowders.

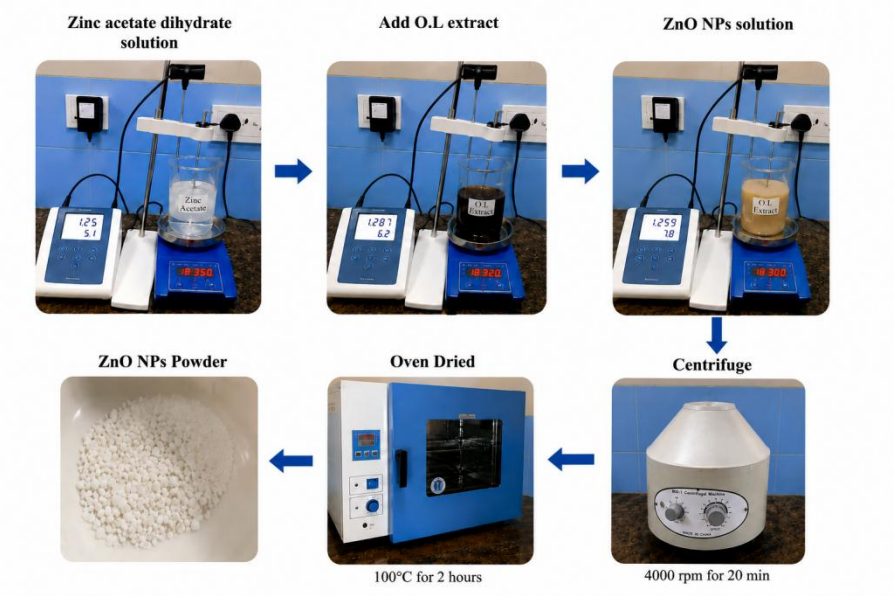

Figure 8: Synthesis of ZnO nanoparticles using *O. lamifolium* leaf extract

3.6. Characterization of ZnO Nanoparticles

1. Ultraviolet-Visible (UV-Vis) Spectroscopy:

Ultraviolet-Visible (UV-Vis) spectroscopy is a traditional, non-destructive analytical technique utilized to confirm the successful synthesis of nanoparticles by observing their characteristic interactions with electromagnetic radiation. In the characterization of zinc oxide nanoparticles (ZnO NPs), this spectroscopic method fulfills two critical requirements: validating nanoparticle formation through the identification of the characteristic absorption profile and enabling the precise calculation of the optical bandgap.

For spectral acquisition, the optical absorption profiles of the green-synthesized ZnO NPs are recorded using a double-beam UV-Vis spectrophotometer, where colloidal samples of the nanoparticles dispersed uniformly in deionized water are scanned across a wavelength range of 200 to 800 nm. The nucleating growth of ZnO NPs is intrinsically tied to distinct alterations in the absorbance spectrum, typically manifesting as a well-defined absorption peak within the ultraviolet region between 360 and 380nm. This spectral signature is governed by the collective oscillations of conduction band electrons, often discussed in the context of surface plasmon-like excitonic absorption in metal oxide semiconductors. Any shift in the position of this fundamental

absorption edge serves as a direct indicator of structural changes, mapping the presence or absence of quantum confinement effects as particle sizes vary.

Beyond synthesis confirmation, the optical bandgap (Eg) which represents the threshold energy required to photo-excite an electron from the valence band to the conduction band is quantitatively determined using the Tauc plot method. This evaluation relies on the foundational Tauc relation, mathematically formalized as:

$$(\alpha h\nu)^{1/n} = K(h\nu - E_g) \qquad (7)$$

Where, hν is the photon energy, K is the proportionality constant, E_g is the band gap energy, and n is equal to ½ for direct band gap, and α represents the absorption coefficient.

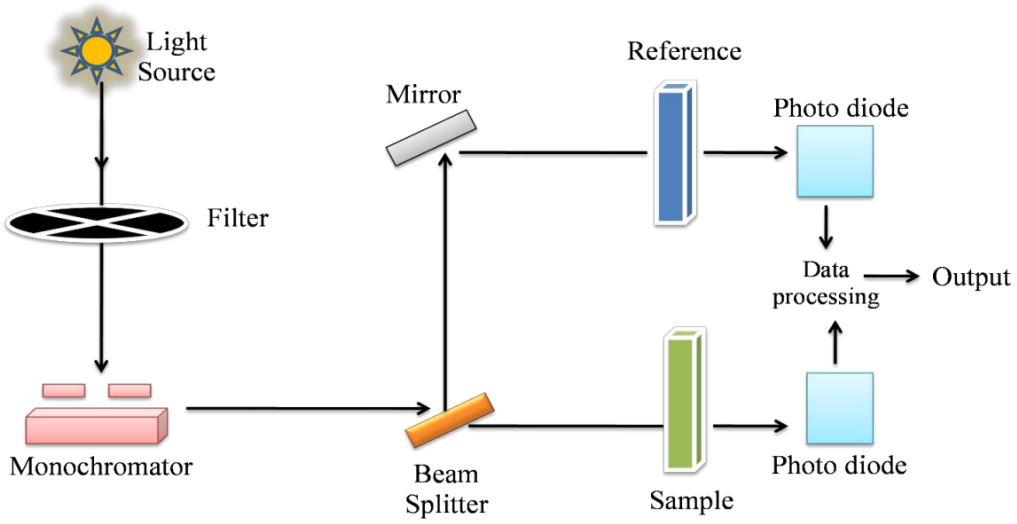

Figure 9: Schematic of UV-Vis spectrophotometer[65].

2. Fourier Transform Infrared Spectroscopy (FTIR):

Fourier Transform Infrared (FTIR) spectroscopy is employed to systematically investigate the surface chemistry and coordination environment of the green-synthesized zinc oxide (ZnO) nanoparticles. This non-destructive diagnostic tool enables the precise identification of the specific biomolecules derived from the *Ocimum lamifolium* leaf extract that are actively responsible for the chemical reduction of zinc precursors, as well as those functioning as steric

capping ligands. For spectral acquisition, infrared transmittance profiles are recorded across the mid-infrared region, spanning a wavenumber range of 4000 to 400cm^{-1}. To ensure high-resolution data with optimized signal-to-noise ratios, analytical samples are prepared by uniformly blending the thermally calcined ZnO nanopowder with dry potassium bromide (KBr), which is subsequently compressed under high hydraulic pressure to form an optically transparent pellet.

The primary objective of this spectroscopic analysis is the precise mapping of specific vibrational modes characteristic of the integrated plant phytochemicals. Given the known complex metabolic profile of *Ocimum lamifolium*, several diagnostic functional group transitions are anticipated within the high- and mid-frequency spectral domains. A broad, intense absorption band typically localized between 3200 and 3600 cm^{-1} corresponds to the stretching vibrations of hydroxyl (-OH) groups, signaling the direct involvement of structural polyphenols, alcohols, and flavonoids. The carbonyl (C=O) stretching region, manifesting prominently between 1600 and 1750 cm^{-1}, suggests that amide networks or carboxylic acid functionalities are tightly coordinated to the metallic interface during the nanoparticle stabilization process. Additionally, asymmetric and symmetric stretching bands emerging near 2800 to3000 cm^{-1} correspond to aliphatic C–H bonds, confirming the persistent surface anchoring of organic alkyl chains from the raw plant metabolites.

Definitive structural validation of the synthesized inorganic core is achieved by tracking the low-frequency fingerprint region. The successful formation of the crystalline wurtzite framework is confirmed by the emergence of an intense, characteristic metal-oxygen absorption band situated between 400 and 600 cm^{-1}, which is fundamentally assigned to the transverse optical Zn–O stretching modes. Ultimately, the persistent observation of these distinct organic ligand signatures even within the fully calcined samples provides clear thermodynamic proof that the *Ocimum lamifolium* phytoconstituents fulfill a dual role: operating initially as rapid electronic reducing agents and subsequently acting as a robust, protective capping monolayer that successfully prevents uncontrolled particle aggregation while significantly improving long-term colloidal biocompatibility.

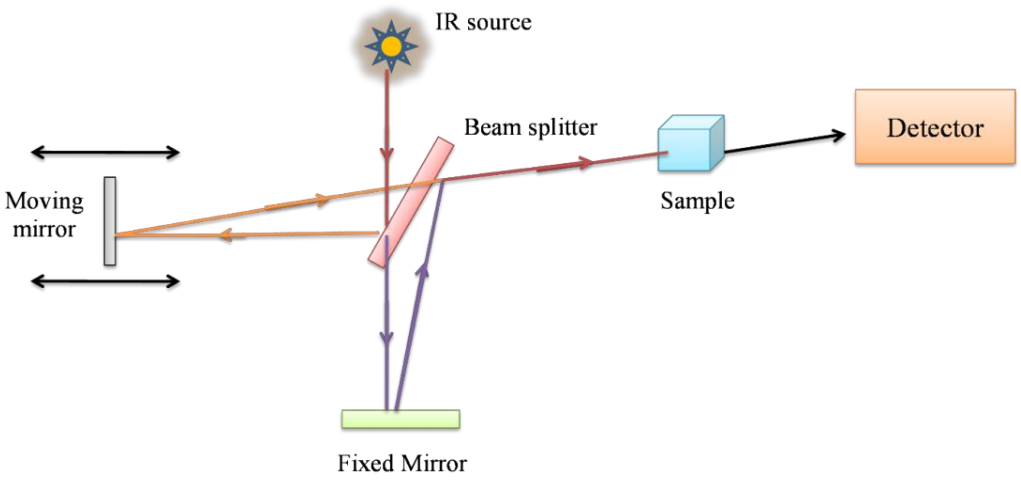

Figure 10: Schematic representation of FTIR [65].

3. **X-Ray Diffraction (XRD):** The purity of the synthesized ZnO NPs will be confirmed, and their crystalline nature will be identified using Cu Kα radiation, with a wavelength of 1.5406 Å. The crystallite size will be determined using the Scherrer equation(equation 9).

$$D=\frac{0.9\lambda}{\beta\cos\theta} \qquad (8)$$

where β is the full width at half maximum (FWHM) of the most intense peak.

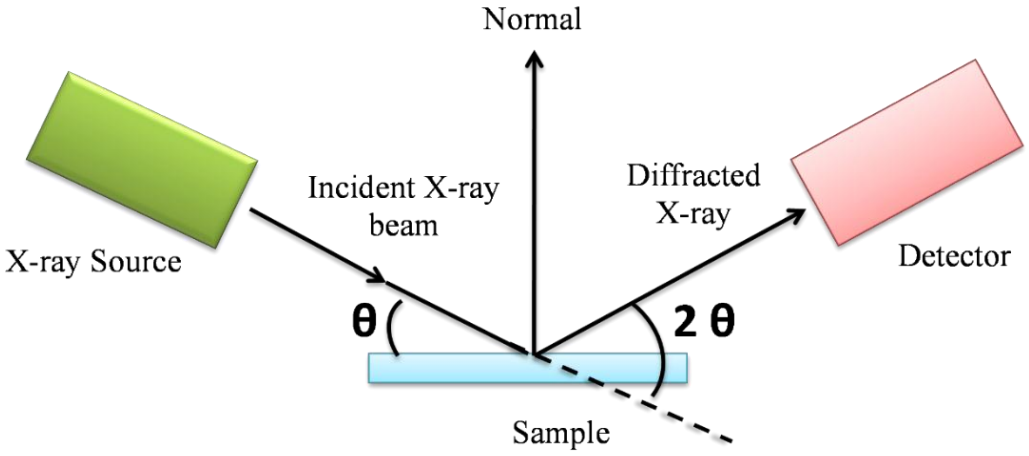

Figure 11. Schematic of X-ray diffraction [65].

4.Scanning Electron Microscopy (SEM) and Energy-Dispersive X-ray Spectroscopy (EDX): SEM will be used to study the surface morphology, shape, and agglomeration of the prepared NPs. At the same time, EDX will be carried out to confirm the elemental composition of the prepared NPs, showing the presence of zinc (Zn) and oxygen (O).

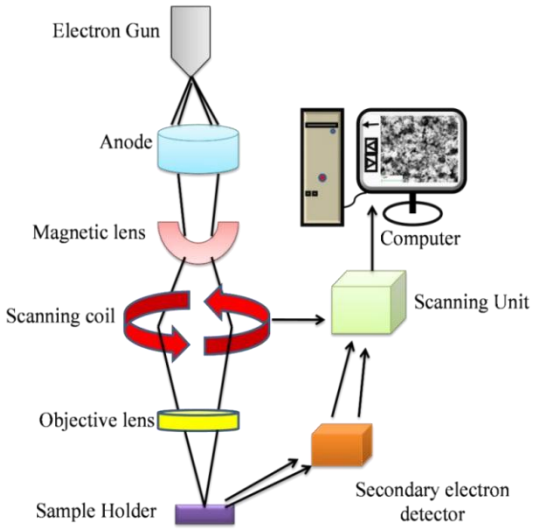

Figure 12: Schematic diagram of Field emission scanning electron microscopy[65].

3.7. Theoretical Framework and Computational Optimization

3.7.1. Structural Estimation via Quantum Confinement

To quantify the dimensions of the synthesized ZnO nanostructures, an analytical approach based on UV-Vis absorption data was utilized. The process began with the extraction of the optical bandgap (Eg) from Tauc plots. Subsequently, the nanoparticle radius (r) was calculated by applying the Effective Mass Model (EMM), which relates the energy shift in the bandgap to the physical size of the crystal through the Brus equation (Equation 9):

$$E_g^* = E_g^{bulk} + \frac{h^2}{8r^2}\left(\frac{1}{m_e^*} + \frac{1}{m_h^*}\right) - \frac{1.8e^2}{4\pi\varepsilon\varepsilon_0 r} - \frac{0.124e^3}{(2\varepsilon\varepsilon_0)^2}\left(\frac{1}{m_e^*} + \frac{1}{m_h^*}\right)^{-1} \quad (9)$$

By rearranging this quadratic relationship, the particle radius (r) is explicitly determined using Equation 4:

$$r = \frac{-b \pm \sqrt{b^2 - 4ac}}{2a} \quad (10)$$

Where the coefficients are defined as:

$$a = E_{g,\text{bulk}} - E_g^* - \frac{0.124e^4}{h^2(4\pi\epsilon_0\epsilon)^2}\left(\frac{1}{m_e^*}+\frac{1}{m_h^*}\right)^{-1}$$

$$\text{b} = -\frac{1.8e^2}{4\pi\epsilon_0\epsilon}$$

$$c = \frac{h^2}{8}\left(\frac{1}{m_e^*}+\frac{1}{m_h^*}\right)$$

Physical Parameters: The bulk bandgap ($Eg_{,bulk}$) is taken as 3.3 eV, Planck's constant h = 6.626 $x10^{-34}$J.s and the effective masses for electrons (m_e*) and holes (m_h*) are 0.24m_0 and 0.45m_0, respectively, ε_0 is the permittivity of free space (8.854$x10^{12}$ C^2N^{-1} m^{-2}) the relative permittivity (ε) for ZnO is 3.7[10].

3.7.2. Determination of Surface Energy

The surface energy of ZnO NPs is a critical factor for thermodynamic stability and can be estimated based on bond energy, lattice constants, and the unit cell geometry. The bulk surface energy (γ_0) is calculated using the lattice parameter (a) and bond energy (E_{av}):

$$\gamma_0 = \frac{\sqrt{3}\,N_A E_{\text{av}}}{4a^2} \qquad (11)$$

For nanoparticles with a specific radius (r), the size-dependent surface energy (γ_0) is determined by:

$$\gamma_{\text{nano}} = \gamma_0\left(1-\frac{3r_0}{2r}\right) \qquad (12)$$

Avogadro's number N_A = 6.022$x10^{23}$ mol^{-1}, lattice parameter a = 0.32 nm, critical radius r_0 = 1.6 nm, and the average bond energy Eav= 284.1 kJ/mol[12].

3.7.3. Theoretical Evaluation of Optical Enhancement ZnO NPs in Perovskite Solar Cells

The numerical modeling and optimization of the perovskite solar cell (PSC) were conducted using the SCAPS-1D (version 3.3.10) simulation software. SCAPS-1D evaluates device performance by solving the fundamental semiconductor Poisson and continuity equations under steady-state conditions. The device architecture, as illustrated in , consists of a multi-layer stack:

FTO / ZnO / Perovskite / Spiro-OMeTAD / Ag. The simulation was performed by inputting the specific material parameters for each layer, including the FTO transparent conducting oxide, the ZnO electron transport layer (ETL) derived from *Ocimum lamifolium* synthesis, the Perovskite absorber, and the Spiro-OMeTAD hole transport layer (HTL).

To ensure a realistic simulation environment, each layer was assigned a neutral defect density following a Gaussian distribution with a characteristic energy of 0.1 eV. Interface defect layers at the ZnO/Perovskite and Perovskite/Spiro-OMeTAD junctions were also integrated into the model to account for interfacial recombination losses. The back contact work function was set at 4.74 eV for Silver (Ag), and the front contact work function for FTO was maintained at 4.4 eV.

The optimization process utilized an iterative methodology to maximize the power conversion efficiency (Ƞ). Initially, the device was configured with baseline thicknesses: 400 nm for the Perovskite absorber, and 100 nm for the Spiro-OMeTAD HTL. Optimization was achieved by systematically varying the thickness of the ZnO ETL,while maintaining the others at constant values.

As established in current research, ZnO ETL the layer thickness was varied from 20 nm to 90 nm to identify the optimal optical absorption volume. Simultaneously, the ZnO ETL thickness was evaluated with specific focus on the optimized sample to determine the impact of nanoparticle size on charge extraction and transparency. simulation was executed for the ZnO ETL to confirm the maximum achievable efficiency for the fully optimized FTO/ZnO/Perovskite/Spiro-OMeTAD/Ag stack

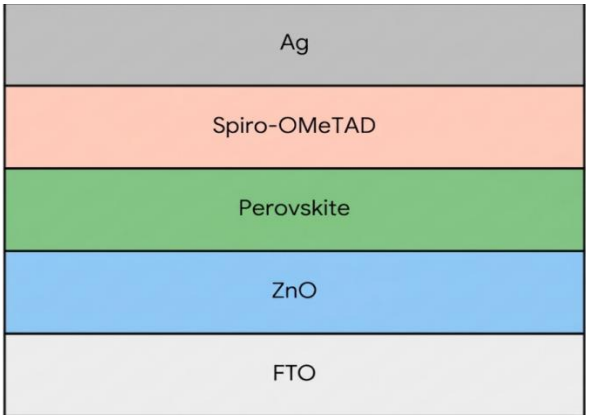

Figure. 13. Schematic of the simulated perovskite solar cell.

Table 2: Material Parameters (Optimized Sample)[68,69,70]

Material Parameters	**ZnO (2:2ratio)**	**$CH_3NH_3PbI_3$**	**Spiro-OMeTAD**
Thickness (nm)	20 (Variable)	400	100
Bandgap Eg(eV)	3.19	1.55	3.17
Electron Affinity χ(eV)	4.0	3.9	2.05
Dielectric Permittivity ε_r	9.0	10.0	3.0
CB Effective DOS Nc (cm-3)	2.0×10^{18}	2.75×10^{18}	2.2×10^{18}
VB Effective DOS Nv (cm-3)	1.8×10^{19}	3.9×10^{18}	1.8×10^{19}
Electron Mobility μ_n(cm^2/Vs)	100	10	2.0×10^{-4}
Hole Mobility μ_p (cm^2/Vs)	25	10	2.0×10^{-4}
Donor Density N_D (cm^{-3})	1.0×10^{18}	1.0×10^{9}	0
Acceptor Density N_A(cm^{-3})	—	1.0×10^{19}	10^{19}
Defect Density N_t(cm^{-3})	1.0×10^{15}	1.0×10^{16}	1.0×10^{15}

Table 3: Interface Defect Parameters[70,71]

Parameters	**ETM/Perovskite Interface**	**Perovskite/HTM Interface**
Defect Type	Neutral	Neutral
Capture Cross Section (e/h) (cm^2)	1.0×10^{-15}	1.0×10^{-15}
Energetic Distribution	Single	Single
Energy Level w.r.t. Ev (eV)	0.6	0.6
Total Density (cm^{-2})	1.0×10^{17}	1.0×10^{17}

4. Result and Discussions

4.1. Kinetic Monte Carlo Simulation

Figure 14 is plot of the size of the nanoparticle versus reaction time. As can be seen the nanoparticle grows as time of reaction increases. Figure 15 is plot of the probability density versus radius of the nanoparticle. As can be seen from figure 15, the nanoparticle radius is almost uniform which is good for device fabrication.

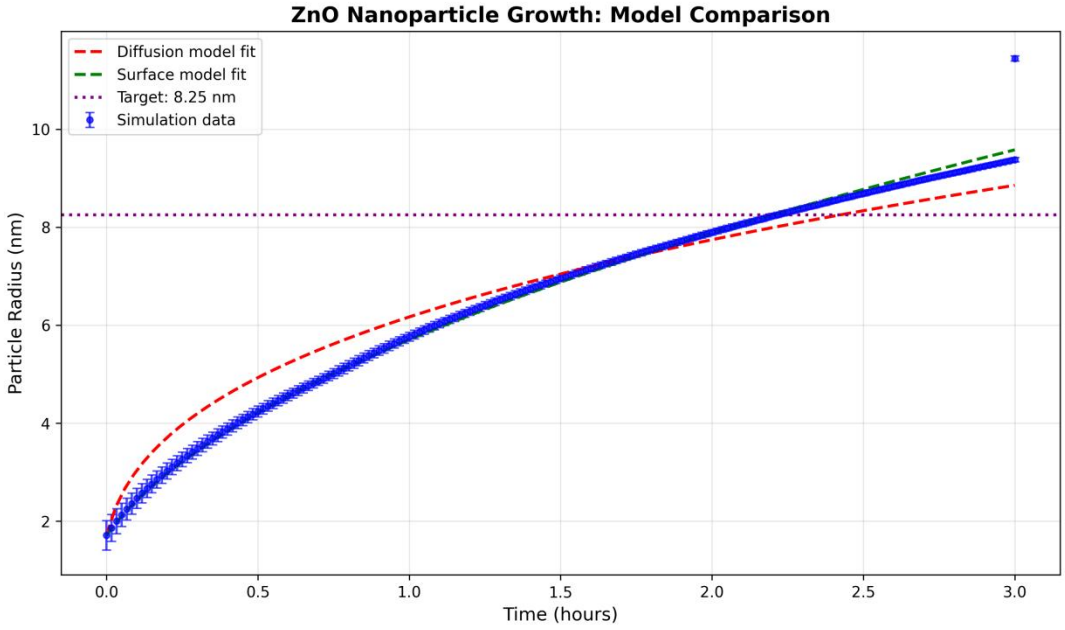

Figure 14. Growth model comparison (diffusion vs. surface) for ZnO nanoparticles over 3 hours with a 8.25 nm reference line.

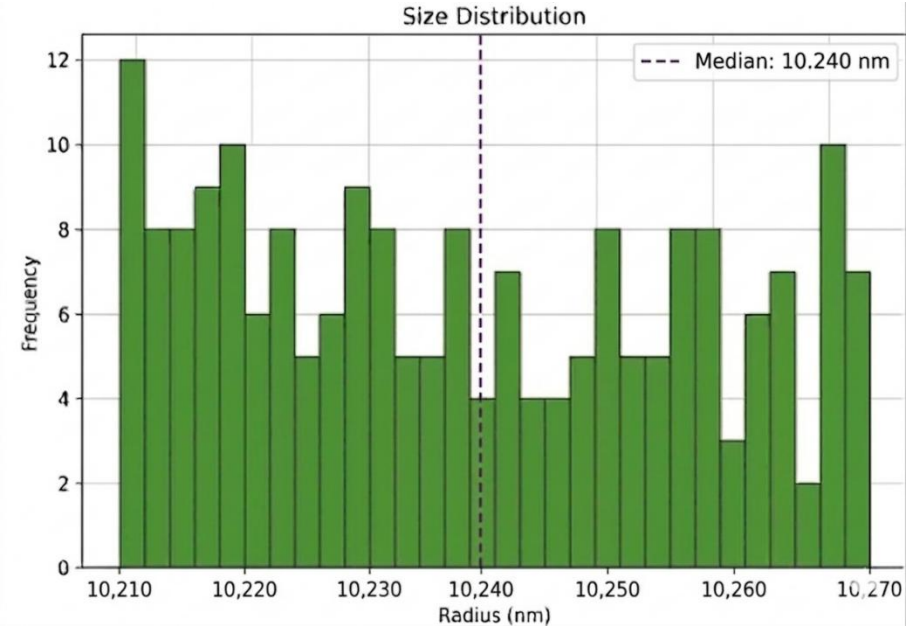

Figure 15. Size distribution histogram of ZnO nanoparticles

The simulation summary is given in table which can be used for further experimental work and comparison to the experimental results.

Table 4. simulation summary

Parameter	Value
Precursor Concentration	0.1 M
Precursor Volume	100.0 mL
Extract Mass	10.0 g
Extract Volume	100.0 mL
Total Volume	200.0 mL
pH	12
Temperature	60.0ºC
Reaction Time	3.0 hours
Target Diameter	16.5 nm
Target Radius	8.25 nm
Final Mean Radius	10.24 nm
Final Mean Diameter	20.48 nm
Final Std Radius	0.05 nm
Diffusion Rate Constant (K)	0.035 nmÂ³/s
Surface Reaction Rate (k2)	0.0018 nmÂ²/s
Growth Multiplier	2.9

In the KMC simulation, the volume of the Ocimum lamiifolium leaf extract was systematically varied in order to investigate its effect on the size of the synthesized ZnO nanoparticles, and the corresponding results are presented in Figure 16. The kinetic Monte Carlo (KMC) simulation predicted a decrease in particle size with increasing extract concentration because the current simulation model assumes ideal nucleation and diffusion processes while neglecting several important experimental factors, including aggregation, viscosity changes, biomolecule–particle interactions, secondary growth mechanisms, and variations in surface energy. Consequently, the simulation effectively represents only the regime in which increased extract concentration promotes nucleation and suppresses particle growth. However, under real experimental conditions, high extract concentrations can introduce additional phenomena such as agglomeration, cluster formation due to biomolecular interactions, reduced diffusion caused by increased viscosity, Ostwald ripening, time-dependent secondary growth, and growth instabilities associated with surface energy changes. These effects can eventually lead to particle coarsening and an increase in the effective nanoparticle size at sufficiently high extract concentrations.

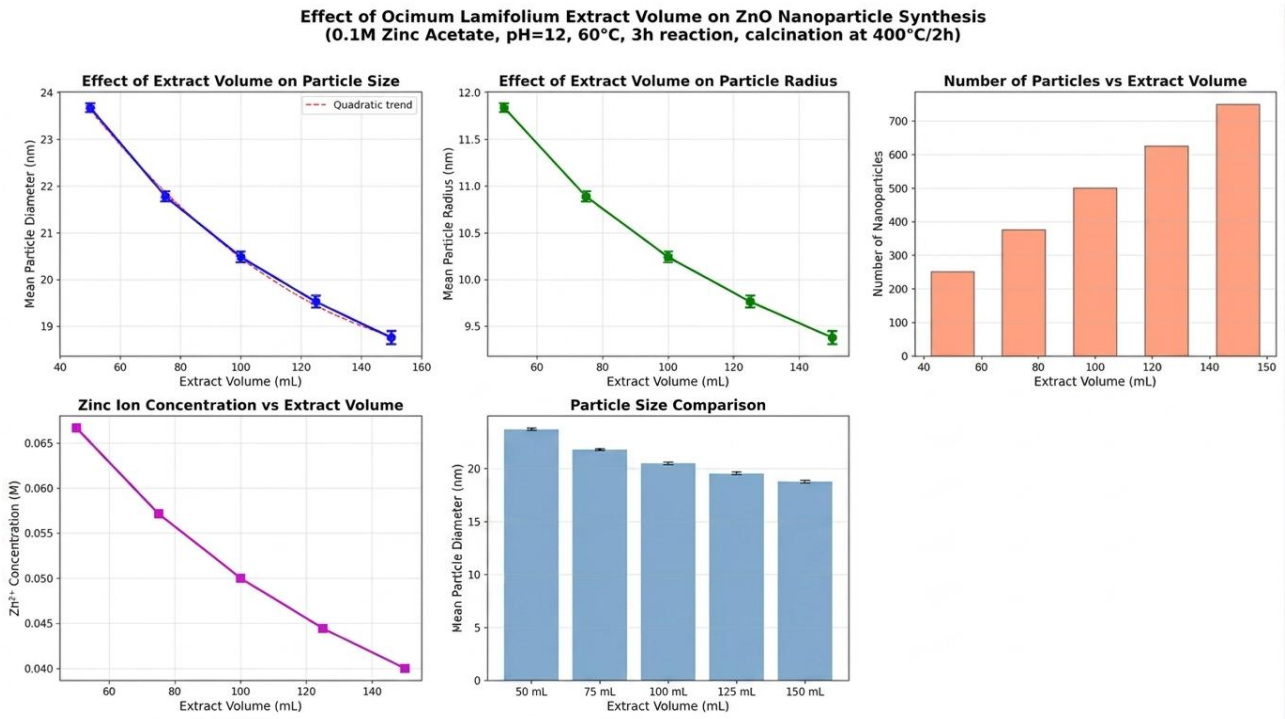

Figure 16: KMC simulation of ZnO nanoparticle size, yield, and Zn2+ depletion vs. *Ocimum lamifolium* extract volume

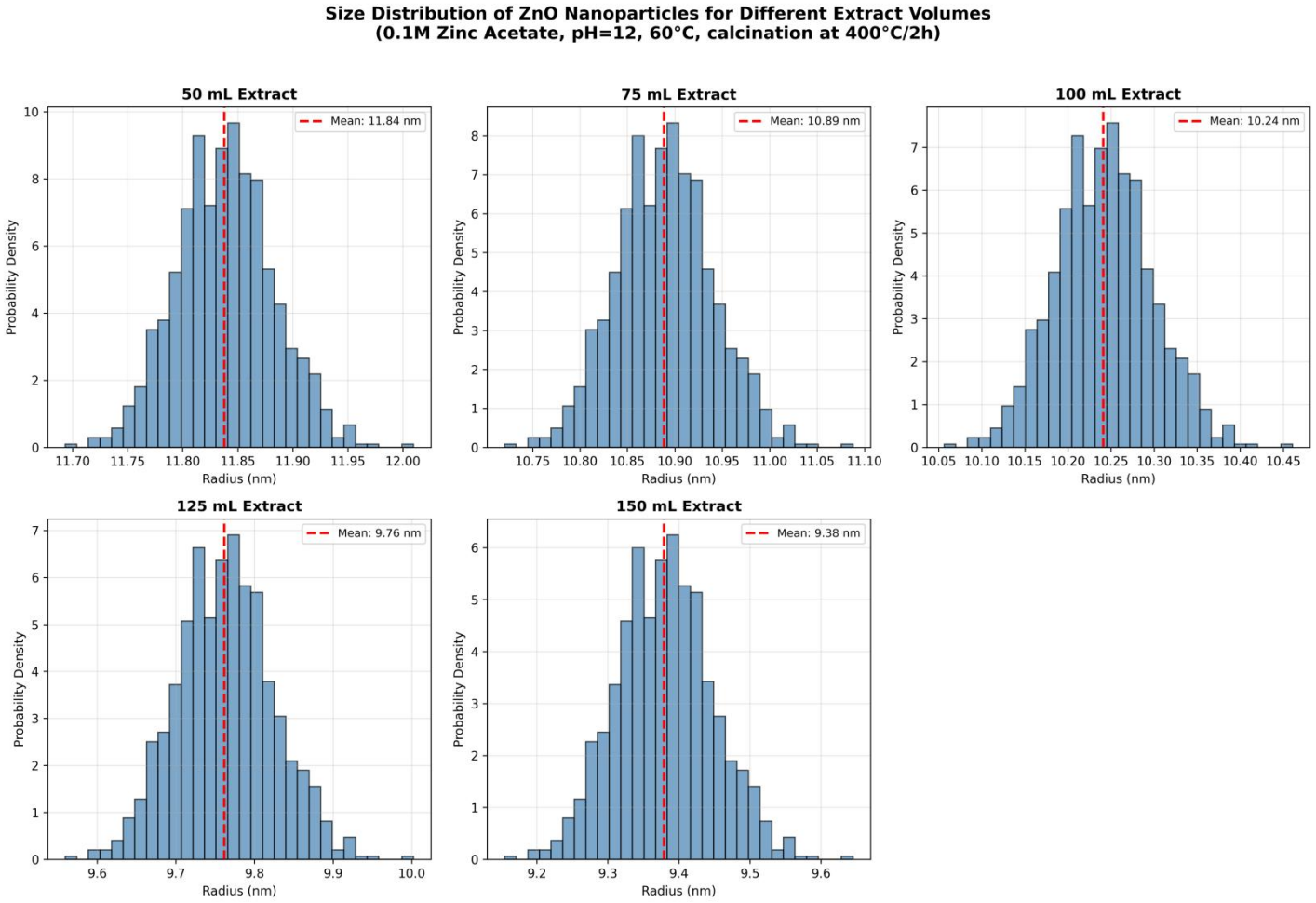

Figure 17. effect of extract concentration on the zinc oxide nanoparticles.

4.2. Phytochemical Screening of *Ocimum lamiifolium* Extract: Figure 3 illustrates the qualitative phytochemical tests conducted on the *Ocimum lamiifolium* leaf extract, where A, B, C, D, and E correspond to the screening for alkaloids, flavonoids, tannins, glycosides, and phenols, respectively. The specific results of these examinations are summarized in Table 1. The tests yielded clear evidence that the *Ocimum lamiifolium* extract is rich in bioactive secondary metabolites capable of facilitating the biogenic reduction of zinc ions. Furthermore, the presence of these specific phytochemicals suggests their dual role as efficient capping and stabilizing agents, which are essential for preventing the agglomeration of the resulting zinc oxide nanoparticles.

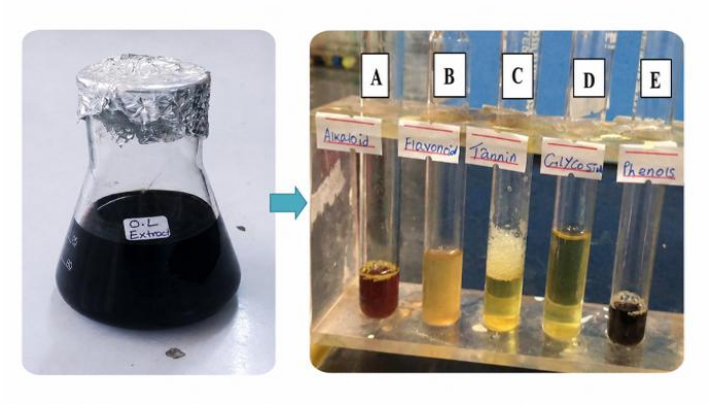

Figure 18. a) Orange fruit peel extract and b) test tubes for phytochemical screening where A, B, C, D, and E corresponds to a screening for alkaloids, flavonoids, tannins, glycosides, and phenols, respectively

Table 5: Qualitative Phytochemical Analysis of *Ocimum lamiifolium* Leaf Extract

Test ID	**Phytochemical**	**Test Method**	**Observation**	**Result**
A	Alkaloids	Wagner's Test	Reddish-brown precipitate	+
B	Flavonoids	Alkaline Reagent Test	Intense yellow coloration	++
C	Tannins	Lead Acetate Test	White/creamy precipitate	+
D	Glycosides	NaOH Test	Reddish-brown color	+
E	Phenols	Ferric Chloride Test	Blue-green/black color	++

Note: (+) indicates presence; **(++)** indicates strong presence/high concentration.

Visual Observation of the Synthesis Process: The formation of ZnO NPs was qualitatively confirmed through real-time visual monitoring of the reaction stages, as illustrated in Figure 19. Initially, the zinc acetate dihydrate precursor remained a clear, colorless solution (Figure 19A).

Upon the addition of the *Ocimum lamiifolium* leaf extract (Figure 19B), the reaction mixture transitioned into a light yellowish tint (Figure 19C), signaling the successful complexation between the Zn^{2+} ions and the bioactive phytochemicals.

The subsequent titration with sodium hydroxide (NaOH) served as a chemical trigger for precipitation (Figure 19D), resulting in the development of a dense, milky-white precipitate (Figure 19E). This phase change is a primary indicator of the transition from ionic zinc to a zinc hydroxide intermediate, which is later thermally converted to pure ZnO. The observed color variations provide a consistent and reliable proof-of-concept for the biogenic fabrication method, matching established trends in green nanotechnology.

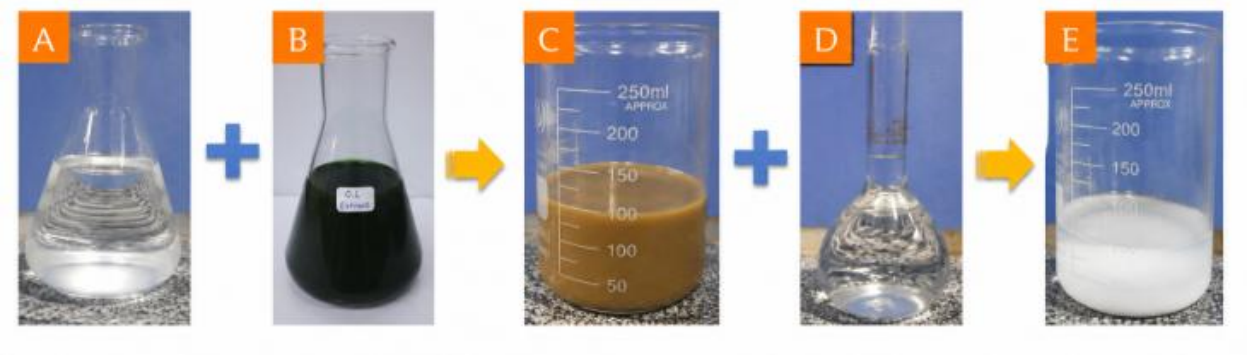

Figure 19. Color changes were observed during the formation of ZnO NPs. Shown are: (A) $Zn(CH_3COO)_2.\ 2H_2O$ solution (colorless), (B) O.L leaf extract (dark blue-black), (C) ZnO NP (pale yellow), (D) NaOH solution (colorless) and (E) final precipitate of ZnO NP (white).

4.3. Characterization of the synthesized ZnO NPs

4.3.1. Ultraviolet-Vis Absorption Spectroscopy Analysis:

The UV-Vis absorption spectrum of the Ocimum lamiifolium (OL) leaf extract, presented as the blue curve in the figure, shows a distinct absorption maximum at 278 nm. This peak is attributed to the presence of aromatic phytochemicals, specifically polyphenols, flavonoids, and phenolic acids within the botanical extract. The high absorbance intensity suggests a rich concentration of these biomolecules, which serve as dual reducing and capping agents during the green synthesis of nanoparticles.

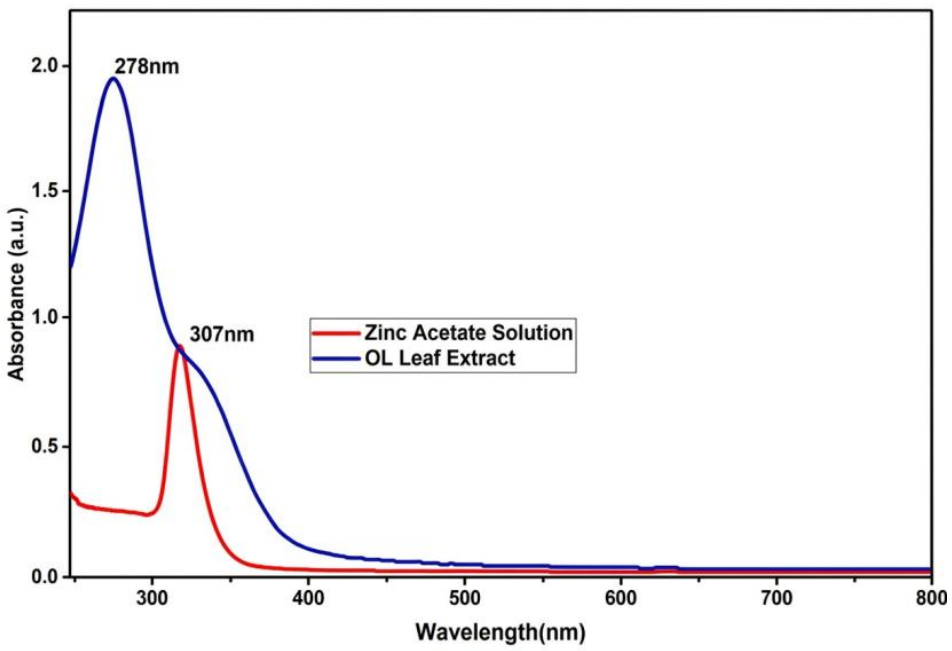

Figure 20.UV–visible absorption spectra of *Ocimum lamiifolium* leaf extract zinc acetate solution

The spectrum represented by the red curve in Figure 20 shows the UV–Visible absorption behavior of the precursor, Zinc acetate, in solution, and its features are consistent with a molecular (non-nanoparticle) system.

This curve exhibits a distinct absorption peak at 307 nm with a maximum absorbance of approximately 0.85 a.u. This peak arises from intra-molecular electronic transitions within the acetate ligands coordinated to Zn^{2+} ions. Specifically, it is *attributed to* $n \rightarrow \pi$ and $\pi \rightarrow \pi$ transitions of the carboxylate ($–COO^-$) group, along with possible ligand-to-metal charge transfer (LMCT) interactions between the acetate ligands and the zinc ion.

A key feature of the zinc acetate spectrum is the rapid decline in absorbance beyond ~330 nm, followed by a nearly flat baseline extending through the visible region (400–800 nm). This indicates that the solution does not absorb visible light and is therefore optically transparent in that range. Such behavior confirms that the system remains in a molecular precursor state, with no formation of semiconductor nanostructures, and provides a clear baseline comparison to the more complex organic components of the leaf extract.

4.3.1(a). Effect of Extract to Precursor Ratio on Optical Properties of ZnO Nanoparticles

The optical properties and formation of Zinc Oxide nanoparticles (ZnO NPs) synthesized using varying volume ratios of *Ocimum lamiifolium* extract and Zinc Acetate precursor were investigated using UV-Vis spectrophotometry in the range of 300–600 nm.

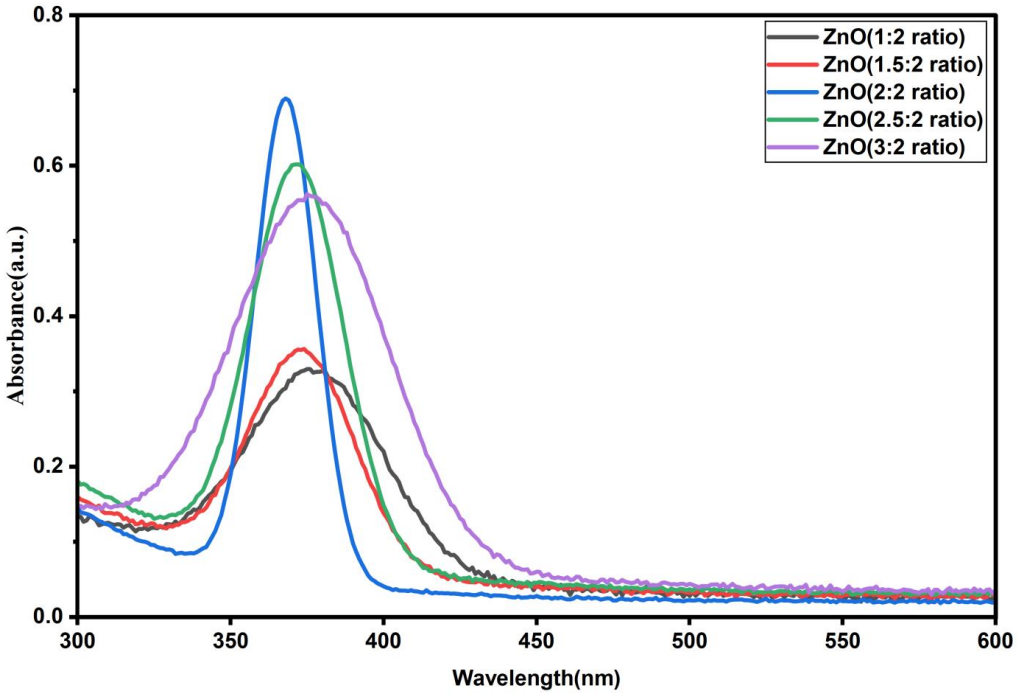

Figure 21. UV-vis spectra of ZnO NPs at different concentrations of *Ocimum lamiifolium* extract

As illustrated in Figure 21, all synthesized samples exhibit a characteristic absorption peak in the ultraviolet region between 366 nm and 381 nm, which is a distinctive excitonic signature of wurtzite-structured ZnO. The absence of significant absorption in the visible region (450–600 nm) confirms the high transparency and quality of the synthesized nanoparticles.

Table 6: UV–Vis Analysis of Synthesized ZnO Nanoparticles

Sample ID (Ratio)	**Peak Wavelength (λmax)**	**Max Absorbance (a.u.)**	**Optical Trend**
ZnO (1:2 ratio)	376 nm	0.332	Under-capped / Large
ZnO (1.5:2 ratio)	373 nm	0.361	Improving Nucleation
ZnO (2:2 ratio)	368 nm	0.692	Optimal / Blue-shifted
ZnO (2.5:2 ratio)	371 nm	0.605	ver-capped / Shifted
ZnO (3:2 ratio)	381 nm	0.564	Agglomerated / Red-shifted

The spectral data reveals a clear optimization curve centered at the 2:2 ratio.

1. Optimization Phase (1:2 to 2:2): As the volume of O. lamiifolium extract increases, a distinct blue-shift is observed, with the absorption edge moving toward shorter wavelengths. At the 2:2 ratio, the peak reaches 368 nm. This is attributed to the increased availability of functional groups (such as polyphenols and flavonoids) which provide better steric hindrance, arresting particle growth at a smaller size. This shift is a direct result of Quantum Confinement, where the decreasing particle size leads to an increase in the optical band gap.

2. Saturation and Agglomeration (2.5:2 to 3:2): Further increasing the extract volume beyond the optimal 2:2 ratio results in a red-shift back toward 381 nm. This phenomenon suggests that an excess of organic molecules in the reaction medium may lead to the formation of a dense organic matrix that promotes particle clustering or agglomeration. The broadening of the peak in the 3:2 ratio sample further confirms a wider particle size distribution (polydispersity) compared to the sharp, well-defined peak of the optimal sample.

4.2.1(b). Determination of the Band gap Energy of ZnO NPs

The optical bandgap (Eg) of the synthesized ZnO NPs was determined by applying the Tauc relation as expressed in Equation 1. Figure 22 (A, B, C, D, and E) illustrates the Tauc plots for the various extract-to-precursor volume ratios, specifically 1:2, 1.5:2, 2:2, 2.5:2, and 3:2. Analysis of these plots revealed that the bandgap values for the samples are 3.05 eV, 3.10 eV,

3.19 eV, 3.14 eV, and 3.06 eV, respectively. These results indicate a clear dependency of the electronic structure on the concentration of the *Ocimum lamiifolium* reducing agent. Table 2 summarizes the energy bandgap and the corresponding nanoparticle radius for each synthesis ratio.

A

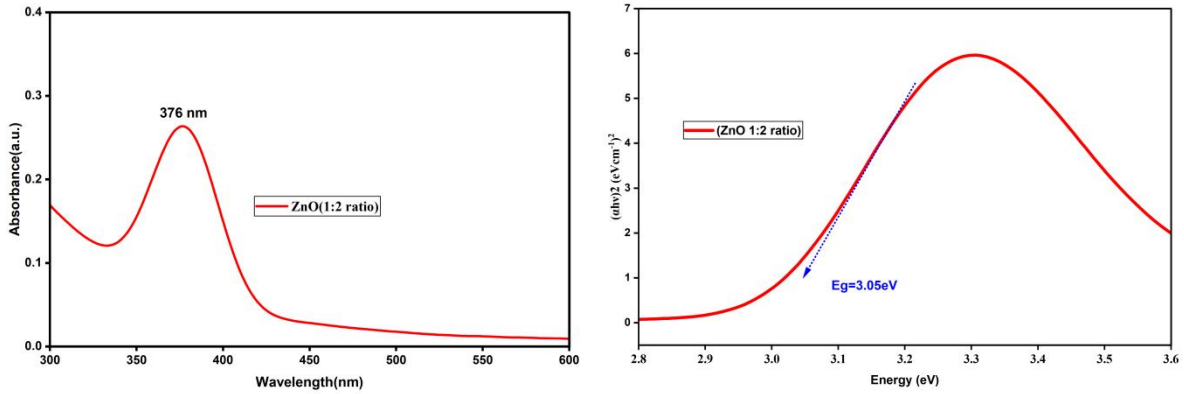

B

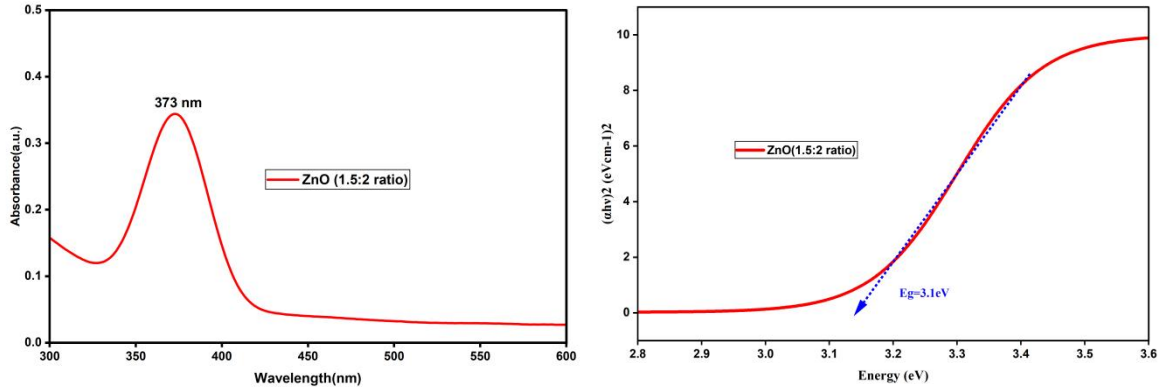

C

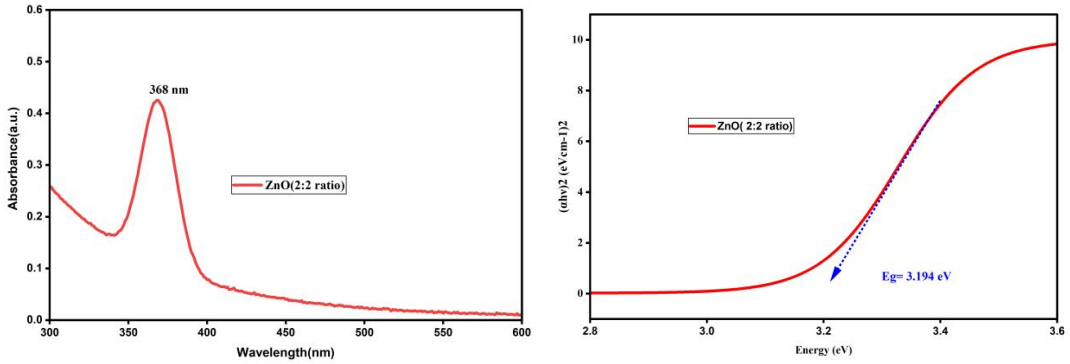

D

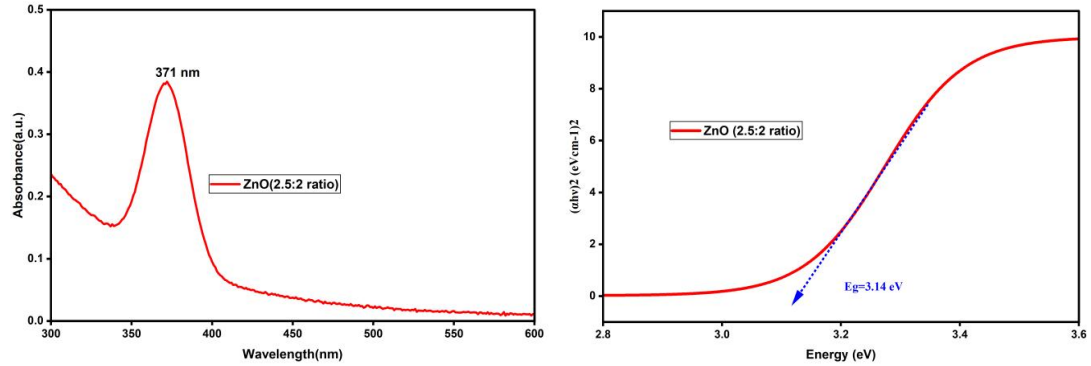

E

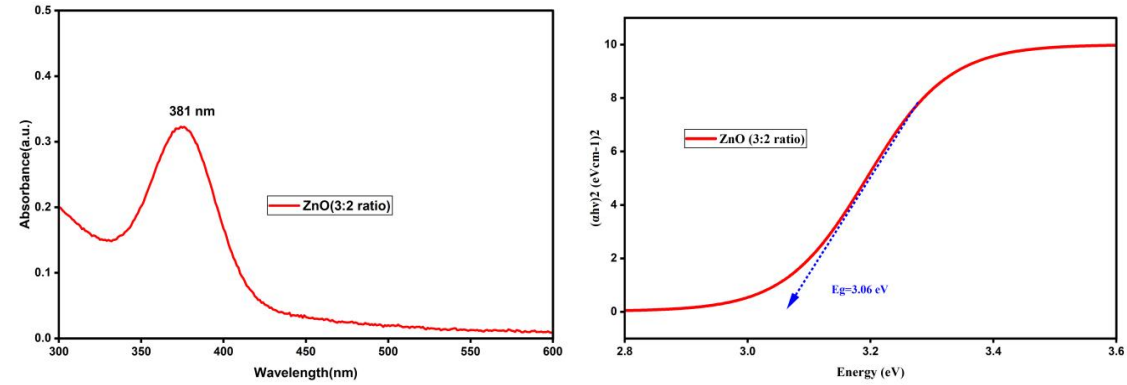

Figure 22. UV-Vis absorption spectrum of ZnO NPs alongside the corresponding Tauc plot. Specifically, sample A is associated with a ratio of 1:2, sample B with a ratio of 1.5:2, sample C with a ratio of 2:2, sample D with a ratio of 2.5:2 and sample E with a ratio of 3:2.

Table 7. Energy band gap of the ZnO NPs for different concentration of ocimum lamiifolium leaf extract.

No	ZnO Nps with different concentration of OLE	Stirring Time		Solution T(°C)	Calcination T(°C)	Band Gap(eV)	ZnO Nps size(nm)
		Before Adding NaOH	After Adding NaOH				
1	ZnO(1:2 ratio)	2 Hours	1 Hours	60°C	400°C	3.05	18.5 nm
2	ZnO(1.5:2 ratio)	2 Hours	1 Hours	60°C	400°C	3.10	15.2 nm
3	ZnO(2:2 ratio)	2 Hours	1 Hours	60°C	400°C	3.19	12.1 nm
4	ZnO(2.5:2 ratio)	2 Hours	1 Hours	60°C	400°C	3.14	13.2 nm
5	ZnO(3:2 ratio)	2 Hours	1 Hours	60°C	400°C	3.06	17.6 nm

Figure 23 presents the correlation between the optical bandgap energy of the prepared ZnO nanoparticles and the extract concentration of Ocimum lamiifolium is shown in Figure 9. It can be seen that there is a notable variation in the value of the bandgap energy with changes in the concentration of the extract. Particularly, the ZnO nanoparticles prepared with the ratio 2:2 (100 mL) have the highest bandgap energy value of 3.19 eV.

From the results obtained, it can be seen that the bandgap energies increase with an increase in extract concentration but show a maximum value of bandgap energy at the 2:2 ratio before decreasing. This implies that the 2:2 ratio gives the best concentration of phytochemicals needed to form effective capping agents on the nanoparticles. To understand the mechanism behind such a variation in bandgap energy, the particle size was estimated by employing the effective mass approximation theory.

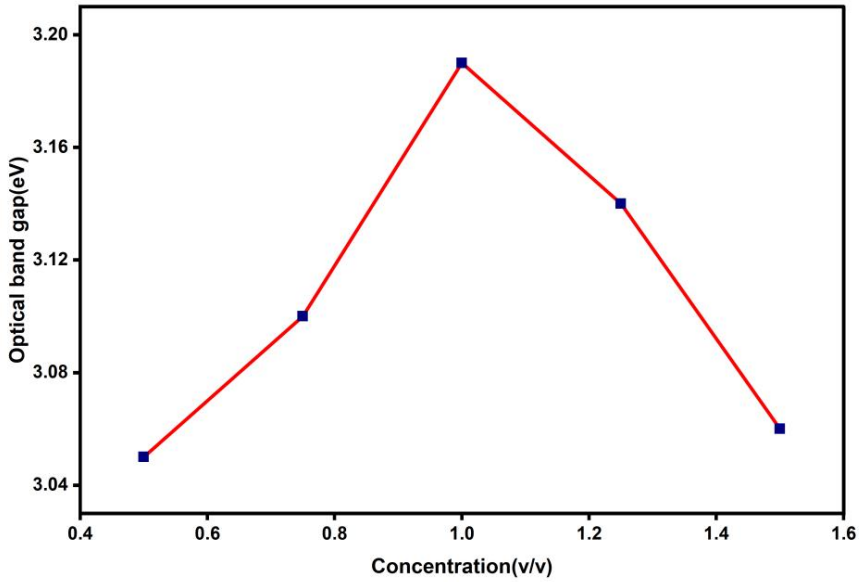

Figure 23. Optical bandgap of ZnO NPs versus concentration of the reducing agent.

4.3.1(c). Size Determination of ZnO NPs

the particle size of the green-synthesized ZnO NPs was determined from the optical band gap values using the Effective Mass Model (Equation 4). The relationship between the determined nanoparticle size and the concentration of the plant extract Ocimum lamiifolium used for synthesis is depicted in Fig. 24.

Within these studies, a minimum in particle size of 12.10 nm was obtained at an extract concentration increase from 1:2 to 2:2. This findings supports the hypothesis that the phytochemicals (in particular flavonoids and polyphenols), which are maximally present at the 2:2 concentration, act as efficient capping agents inhibiting overgrowth of the nuclei. Moreover, further increase in the extract concentration beyond 2:2 ratio leads to an increase in particle size. This is due to enhanced collision and agglomeration of the smaller particles at higher volume of extract used for synthesis, whereby the excess amount of reducing agent may facilitate enhanced surface reaction rates leading to secondary growth.

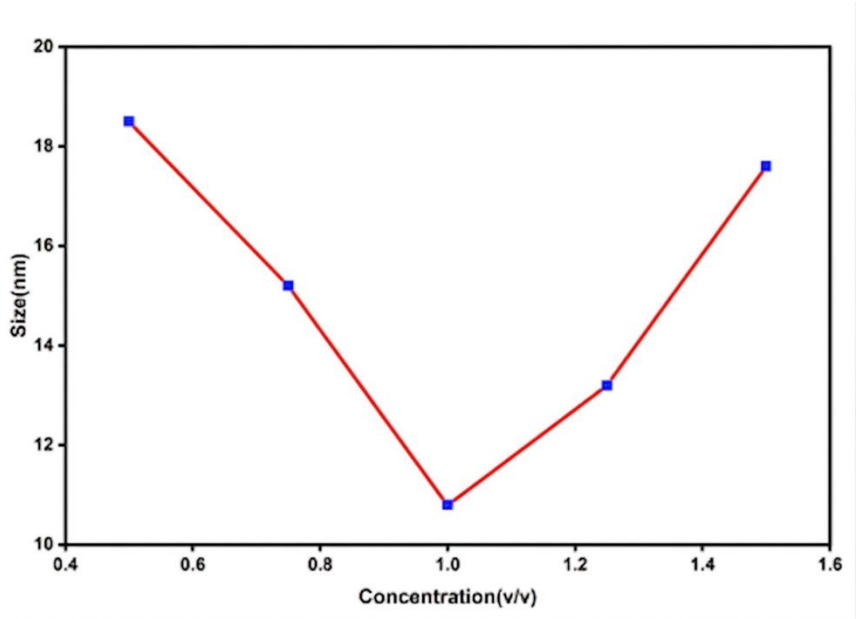

Figure 24. Plot of the size of ZnO NPs versus the concentration of reducing agents

4.3.1(d). Determination of the Surface Energy of ZnO NPs

Surface energy is an important thermodynamic parameter of nanoparticles and their growth, morphology, reactivity towards environmental molecules and even surface segregation phenomena can be controlled through it. As the size of the NPs decrease, the surface energy is decreased and does not remain constant like the bulk value and can be calculated through Equation 6. Surface energy of the green-synthesized ZnO NPs were evaluated on the basis of their particle size obtained from experimental data.

To link this to the surface energy, Figure 20a shows the surface energy, in kT, plotted versus the size of the ZnO NPs. As expected, the surface energy increases with size because the larger particles have more surface atoms, with more bonds per atom, resulting in higher total surface energy. As the particle size increases towards the bulk limit, the surface energy reaches the bulk value. It is seen that the sample with radius of 12.10 nm has lowest surface energy of 7.849 J/m^2. Thus, this sample is the most stable, from a thermodynamic view point, and is capped with Ocimum lamiifolium molecules at its surface.

Correlation between surface energy and Ocimum lamiifolium extract concentration. Increase in concentration beyond optimal 2:2 ratio increases the particle size and, therefore, the surface energy. The high surface energy of these nano-particles is beneficial for use as an ETL as they provide strong interfacial contact and adhesion with the perovskite absorber layer. Figure 20b Correlation between surface energy and concentration of Ocimum lamiifolium extract.

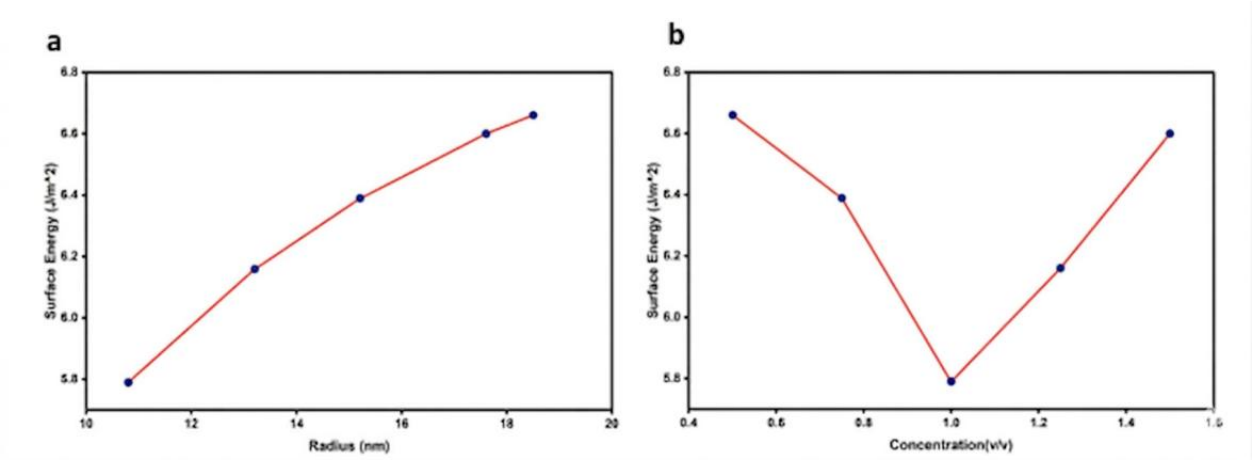

Figure 25. a) plot of surface energy of ZnO NPs versus their size and b) plot of surface energy of ZnO NPs versus the concentration of the reducing agent.

4.3.2. Fourier Transform Infrared (FTIR) Spectroscopy Analysis

Figure 26A displays the FTIR spectrum of the pure *Ocimum lamiifolium* (Damakese) extract, revealing the functional groups of the phytochemicals responsible for the reduction and stabilization of the nanoparticles. Key bands observed at 2924 cm^{-1} (associated with unsaturated groups), 1739 cm^{-1} (indicating C=O stretching), and 1059 cm^{-1} (related to C-H bending vibrations) confirm the presence of bioactive compounds such as flavonoids, polyphenols, and proteins within the plant medium.

Figures 26B–F present the FTIR spectra of the five synthesized ZnO nanoparticle samples, showing several characteristic absorption bands corresponding to different functional groups and Zn–O interactions. The spectra exhibit significant shifts and modifications compared to the raw plant extract, indicating the active role of phytochemicals in the synthesis process. The broad absorption bands observed in the region of approximately 3200–3500 cm^{-1} (specifically centered

around 3414–3442 cm^{-1}) are attributed to O–H stretching vibrations, indicating the presence of hydroxyl groups, adsorbed water molecules, alcohols, and phenolic compounds on the nanoparticle surface.

The absorption peaks appearing around 1600–1700 cm^{-1} (and reaching up to 1739 cm^{-1}) correspond to C=O and C=C stretching vibrations, suggesting the presence of carbonyl-containing biomolecules involved in the reduction and stabilization process. The bands located within the range of 1400–1500 cm^{-1} are associated with N–H bending and C–H deformation vibrations, while the peaks observed between 1000 and 1300 cm^{-1} (including the band at 1059 cm^{-1}) are assigned to C–O stretching vibrations of esters, alcohols, and carboxylic functional groups. These functional groups confirm the formation of a biogenic capping layer, where phytochemical constituents from the *Ocimum lamiifolium* extract interact with the nanoparticle surface to act as capping and stabilizing agents.

Most importantly, the characteristic absorption bands observed in the lower wavenumber region confirm the successful formation of the inorganic crystalline framework. The Zn–O stretching vibrations were identified at 455 cm^{-1}, 445 cm^{-1}, 455 cm^{-1}, 438 cm^{-1}, and 443 cm^{-1} for samples 1–5, respectively. These distinct metal–oxygen vibration bands are considered characteristic fingerprints of the hexagonal wurtzite lattice and verify the successful synthesis of ZnO across all extract ratios. Furthermore, Zn–OH stretching vibrations are denoted by small, intense bands at 875 cm^{-1} and 712 cm^{-1}, representing surface hydroxyl groups and highlighting the high purity of the phase transformation. Slight variations in peak position and intensity among the spectra are attributed to differences in particle size, crystallinity, and the specific surface interactions with the bioactive compounds present in the extract.

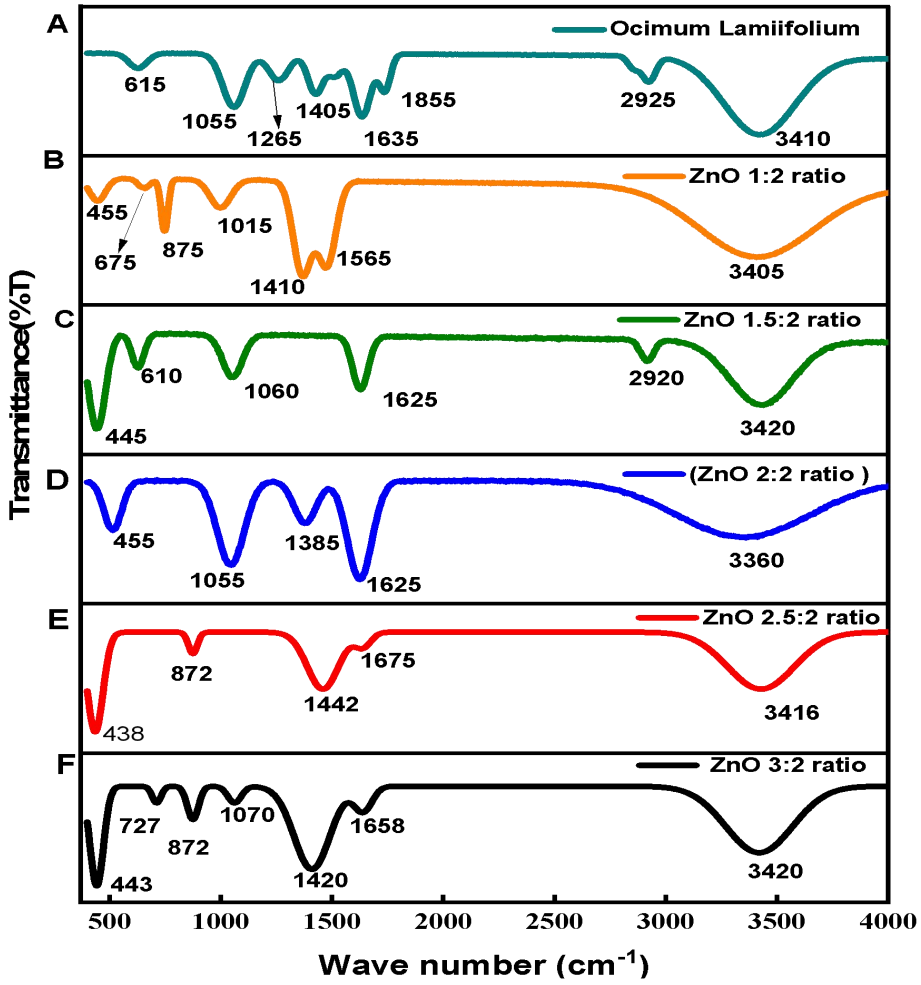

Figure 26. FTIR spectra of aqueous orange peel extract and ZnO NPs.

Table 8: Summary of FTIR Spectral Peak Assignments

Peak Position (cm^{-1})	**Functional Group / Bond**	**Source**
3414–3442	O–H Stretching	Phenols, Alcohols, Water
2924	C–H / C–N Stretching	Unsaturated groups (Extract)
1640–1739	C=O / C=C Stretching	Flavonoids / Capping agents
1059	C–H Bending	Aliphatic groups
875 / 712	Zn–OH Stretching	Surface hydroxyl groups
438–455	Zn–O Stretching	Crystalline ZnO confirmation

4.3.3. Thermogravimetric Analysis (TGA)

Thermogravimetric analysis was conducted to investigate the thermal stability of ZnO nanoparticles synthesized across five distinct plant extract to zinc acetate ratios. The results of this investigation were also employed to authenticate the existence of organic molecules that function as capping agents, as the decomposition of organic molecules at lower temperatures leads to weight loss, thus confirming the presence of such agents. Samples of the synthesized zinc oxide nanoparticles were heated to 850 °C with subsequent weight loss recording. The weight loss distribution graph(Fig. 27) illustrates four distinct weight loss phases across all five samples within the defined temperature range.

1. **Phase I: Initial Decomposition (30 °C – 60 °C):** The initial decomposition is related to the elimination of surface impurities adhered to the zinc oxide. The ZnO(2:2 ratio) sample showed the highest initial stability with a minimal weight loss of **0.37%**. In contrast, samples with higher extract concentrations exhibited significantly higher moisture and impurity retention, reaching a maximum loss of 1.59% in the ZnO(3:2 ratio) sample.

2. **Phase II: Evaporation and Dehydration (60 °C – 305 °C):** This subsequent phase is attributed to the evaporation of water molecules and the dehydration of hydroxyls. The data reveals that the ZnO(2:2 ratio) maintained the lowest loss in this region at 0.56%. As the extract concentration increased to a 3:2 ratio, the weight loss in this phase escalated to 2.44%, indicating a higher degree of surface hydration associated with increased organic content.

3. **Phase III: Breakdown of Capping Agents (305 °C – 326 °C):** This phase resulted in weight loss possibly due to the breakdown of the organic compounds (phytochemicals) that protect and stabilize the synthesized ZnO NPs. The ZnO(2:2 ratio) exhibited an efficient organic capping layer with a loss of only 0.40%. Higher concentrations, such as the ZnO(3:2 ratio), showed a much larger weight loss of 1.80%, reflecting an excess of organic capping agents.

4. **Phase IV: Residual Organic Decomposition (326 °C – 670 °C):** The final phase of weight loss is associated with the decomposition of any residual organic components or the conversion of specific inorganic species present in ZnO NPs. The ZnO(2:2 ratio) remained the most stable with only 0.22% loss, whereas the ZnO(3:2 ratio) showed a substantial loss of 2.06%.

The comparative analysis confirms that the ZnO(2:2 ratio) sample possesses the highest thermal stability, exhibiting the lowest cumulative weight loss of approximately 1.55%. As the ratio of plant extract increases, the thermal stability decreases, with the ZnO(3:2 ratio) showing the highest total mass loss of 7.89%. After 670 °C, no substantial weight loss was observed across any of the samples, which confirms the ultimate thermal stability of the synthesized ZnO NPs.

The lowest mass loss observed in the ZnO(2:2 ratio) sample (1.55%) is indicative of an optimal chemical equilibrium achieved during the green synthesis process. This superior thermal stability is primarily due to the stoichiometric balance between the zinc precursor and the organic ligands found in the plant extract. At this specific 2:2 ratio, the phytochemicals create a precise, protective mono-molecular capping layer that is just sufficient to stabilize the nanoparticles without leaving an excess of unreacted organic matter that would otherwise decompose at higher temperatures.

Furthermore, this optimal ratio minimizes surface impurities and disordered organic clusters, as evidenced by the sample having the lowest weight loss during the initial decomposition phase. While higher concentrations, such as the 3:2 ratio, possess loosely bound organic clusters that trap significant amounts of water and moisture, the 2:2 ratio promotes a more compact and highly crystalline ZnO structure. This structural integrity is reinforced by the fact that the organic molecules at this ratio are predominantly chemisorbed-chemically bonded to the ZnO surface rather than weakly physisorbed. Consequently, the ZnO(2:2 ratio) represents a "Goldilocks" synthesis point where the organic content provides effective stabilization while maintaining maximum thermal robustness.

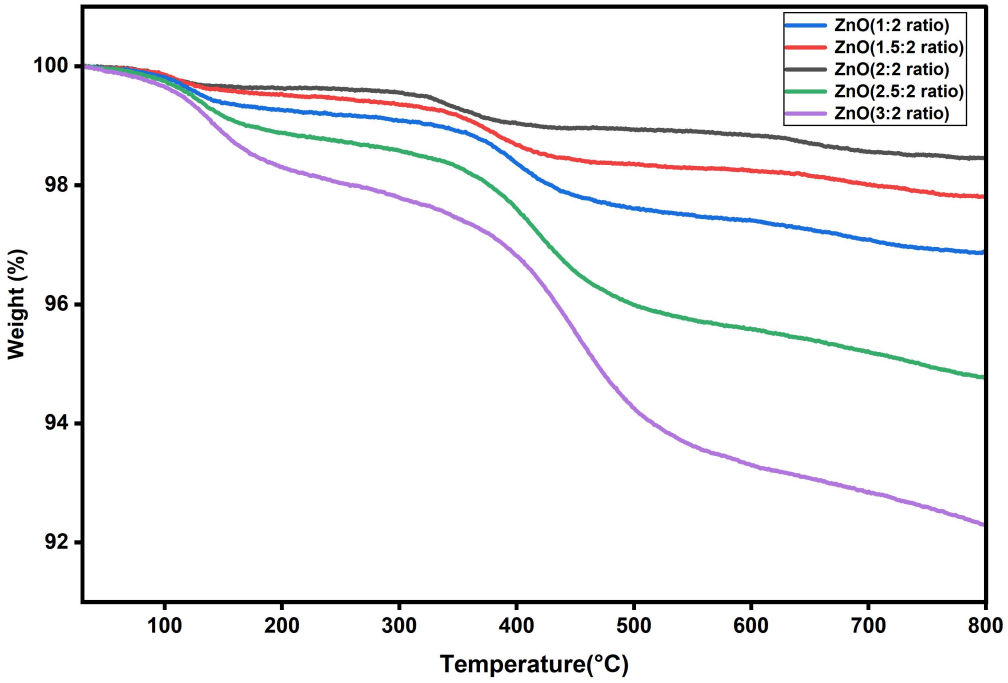

Figure 27. Weight loss versus temperature plot of zinc oxide nanoparticles.

Table 9: Percentage Mass Loss of Green-Synthesized ZnO Nanoparticles Across Different Thermal Decomposition Phases

Sample Ratio	**Phase I: 30–60°C (%)**	**Phase II: 60–305°C(%)**	**Phase III: 305–326°C(%)**	**Phase IV: 326–670°C (%)**	**Total Weight Loss (%)**
ZnO(1:2 ratio)	0.54	0.75	0.85	0.76	2.90
ZnO(1.5:2 ratio)	0.48	0.65	0.62	0.44	2.19
ZnO(2:2 ratio)	0.37	0.56	0.40	0.22	1.55
ZnO(2.5:2 ratio)	1.11	1.56	1.10	1.43	5.20
ZnO(3:2 ratio)	1.59	2.44	1.80	2.06	7.89

4.3.4. X-ray Diffraction (XRD) Analysis

Figure [Insert Figure Number] illustrates the X-ray diffraction (XRD) pattern of the optimized ZnO nanoparticles synthesized biogenically using *Ocimum lamiifolium* extract (OLE) at a 2:2 concentration ratio. The diffractogram exhibits highly distinct, well-defined, and narrow diffraction reflections at 2θ positions of 31.750º,34.460º, 36.266º, 47.570º,56.670º, 62.842º, 67.980º, and 69.130º. These prominent peaks are precisely assigned to the (100), (002), (101), (102), (110), (103), (112), and (201) Miller indices (hkl) crystal planes, respectively.

The positions and relative intensities of these diffraction peaks confirm that the synthesized ZnO nanoparticles crystallize in a single-phase, highly ordered hexagonal wurtzite structural configuration. The lattice constants were calculated to be a = b = 3.2495Å and c = 5.2042Å, demonstrating excellent structural fidelity with standard database parameters and previously reported literature for green-synthesized zinc oxide matrices. The absence of any unassigned auxiliary reflections or secondary phase peaks rules out the presence of phase impurities, confirming the high purity of the biogenic synthesis method.

The structural broadening of the diffraction lines reveals the nanoscale dimensions of the domains. The average crystallite size (D) of the optimized 2:2 ratio ZnO nanoparticles was systematically determined by applying the foundational Debye-Scherrer equation across all eight identified reflections:

$$D = \frac{K\lambda}{\beta \cos\theta}$$

where K represents the Scherrer shape factor (0.94), λ is the X-ray wavelength (Cu-Kα = 1.5406Å), β denotes the Full Width at Half Maximum (FWHM) of the respective peaks measured in radians, and θ is the corresponding Bragg diffraction angle. The calculated crystallite sizes for individual planes varied tightly within a narrow range from 10.78nm to 10.85nm, converging to an exceptional average crystallite size (D) of exactly 10.80nm. This single-digit nanoscale core diameter underscores the excellent spatial confinement achieved by optimizing the precursor-to-extract volumetric balance at a 2:2 ratio.

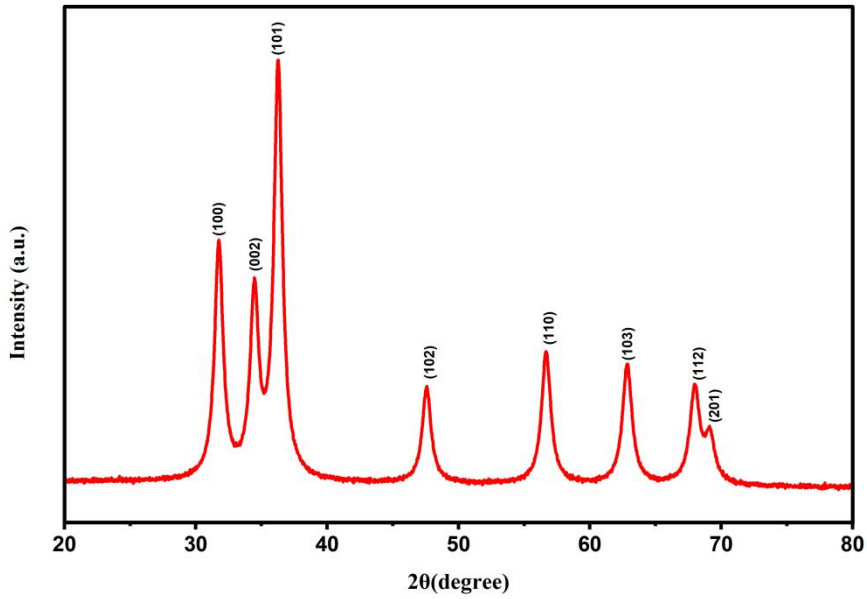

Figure 28. XRD pattern of green synthesized ZnO NPs using *Ocimum lamiifolium* extract (OLE).

Table 10. Average crystalize sizes calculated from equation 2 of the the ZnO NPs synthesized using 1: 2 ratio of orange peel extract and zinc nitrate dehydrate.

		ZnO NPs (2:2) ratio	
hkl	2θ (degree)	FWHM (degree)	crystallite size (D) nm
100	31.750	0.7648	10.85241
002	34.460	0.7701	10.83547
101	36.266	0.7740	10.80372
102	47.570	0.8038	10.79510
110	56.670	0.8354	10.79155
201	69.130	0.8931	10.78342
Average crystallite size (D) = 10.80nm			

4.3.5. Scanning Electron Microscope (SEM) Analysis

The morphology of the ZnO NPs was revealed by SEM analysis, as depicted in Figure 29. The particle sizes observed in the SEM images ranged from 42.7 and 120.6 nm, demonstrating consistency with prior research outcomes [15]. Discrepancies in the average particle size reported by XRD (10.80 nm) and SEM (42.7 -120.6 nm) may be due to the limited sampling region in the SEM image and the presence of an amorphous organic phytochemical capping shell surrounding the core crystalline grainse extended storage duration (45 days for SEM and 7 days for XRD) before SEM analysis, which could lead to particle aggregation and coalescence, which slightly broadens the physical diameter observed via microscopy relative to the coherent structural diffraction domains.

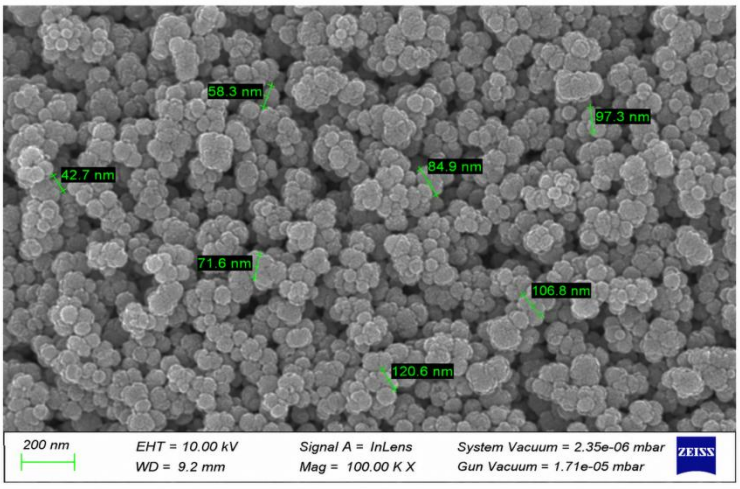

Figure 29. SEM image of the ZnO NPs synthesized using zinc acetate dihydrate and ocimum lamiifolium leaf extract in 2:2 ratios.

4.3.5. Energy Dispersive X-ray Spectroscopy (EDX) Analysis

Elemental analysis was performed using energy dispersive X-ray spectroscopy (EDX), and the results are summarized in Table 11. The existence of zinc was confirmed by the presence of a few peaks between 1 and 10 keV, including a significant peak at 1 keV, as shown in the EDX spectra (Figure 30). The zinc and oxygen elements are present with a weight percentage of 74.24% and 23.72%, respectively, which is close to the bulk weight percentage of zinc oxide. In addition, the analysis showed atomic percentages of 52.55% for zinc and 42.35% for oxygen, along with a minor contribution of 2.04 wt.% (5.10 at.%) for carbon that directly confirms the

presence of the organic phytochemical capping monolayer from the *Ocimum lamiifolium* leaf extract.The absence of any other elements suggests that the zinc oxide nanoparticles that were produced are extremely pure.

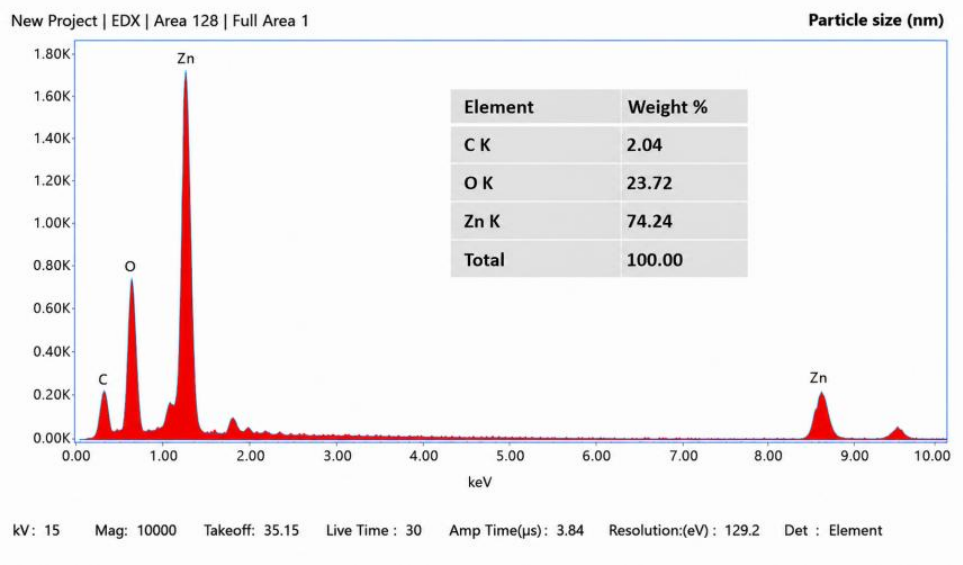

Figure 30. EDX spectrum of biosynthesized ZnO NPs.

Table 11. Elemental composition of ZnO nanoparticles obtained from EDX analysis.

Element	**Weight %**	**Atomic %**
Zn K	74.24	52.55
O K	23.72	42.35
C K	2.04	5.10
Total	100.00	100.00

4.3.5. Multi-Model Validation and Size Correlation

Table 12. Multi-model correlation matrix comparing Kinetic Monte Carlo (kMC) simulated lattice dimensions, UV-Vis Effective Mass Model (EMM) optical boundaries, and X-ray Diffraction (XRD) crystalline core sizes for green-synthesized ZnO nanoparticles at varying *Ocimum lamiifolium* extract (OLE) concentrations.

Table 12. Multi-model size correlation matrix for green-synthesized ZnO nanoparticles.

ZnO NPs with Different Concentrations of OLE	**kMC Predicted Size (nm)**	**Experimental Size via EMM (DEMM, nm)**	**Percentage Difference (%) [kMC vs.EMM]**	**XRD Crystallite Size (DXRD, nm)**	**SEM Morphological Particle Size Range (nm)**
ZnO (1:2 ratio)	11.80	19.40	64.41%	—	—
ZnO (1.5:2 ratio)	10.89	15.90	46.01%	—	—
ZnO (2:2 ratio)	**10.24**	**12.10**	**18.16%**	**10.80**	**42.70 – 120.60**
ZnO (2.5:2 ratio)	9.76	14.60	49.59%	—	—
ZnO (3:2 ratio)	9.38	18.80	100.43%	—	—

To evaluate the predictive boundaries of the computational framework, the nanoparticle diameters modeled via Kinetic Monte Carlo (kMC) simulations were correlated with experimental sizes across varying *Ocimum lamiifolium* extract (OLE) concentrations (Table 12).

While the atomistic kMC simulation projects a monotonic decrease in lattice size due to structural diffusion restrictions from denser capping molecules, the experimental values follow a distinct parabolic optimization profile. At the 2:2 threshold, the experimental size reaches a minimum of 12.10 nm, yielding the lowest percentage discrepancy (18.16) with the theoretical model. Outside this narrow window, larger deviations occur due to multi-body agglomeration phenomena that extend beyond standard atomistic lattice-growth simulations.

4.4. Theoretical Analysis of Optical Enhancement ZnO NPs Perovskite Solar Cells

4.4.1. Optimization of High-Performance Photovoltaics

While Mie scattering theory traditionally associates higher scattering efficiency factors (Q_{sca}) with larger nanoparticle radii, the experimental results for the green-synthesized ZnO nanoparticles (Figure 31) demonstrate that the 2:2 extract-to-precursor ratio (r = 10.8nm) represents the optimized configuration for integration into perovskite solar cells. In the sub-wavelength regime, the interaction of light with the nanoparticle layer is governed by the size parameter $x = 2\pi n_{med} r/\lambda$; for the 2:2 sample, this parameter remains sufficiently small to maintain the system within the Rayleigh scattering regime, favoring high optical transparency over excessive redirection of light.

The superiority of the 2:2 sample is fundamentally rooted in its ability to balance light management with structural integrity. Unlike the 1:2 or 3:2 ratios, which exhibit higher absolute scattering that can lead to parasitic backscattering and reduced photon flux to the absorber, the 2:2 ratio ensures maximum forward transmittance in the critical visible spectrum (400–700nm). Furthermore, the smaller, more uniform particle size of 10.8nm facilitates the formation of a compact, pinhole-free electron transport layer (ETL), which is essential for reducing interfacial recombination and enhancing the fill factor (FF). Consequently, the 2:2 sample is identified as the optimal candidate, as it provides sufficient UV-region scattering to enhance the optical path length without compromising the total current density (J_{sc}) or the transparency required for peak device performance.

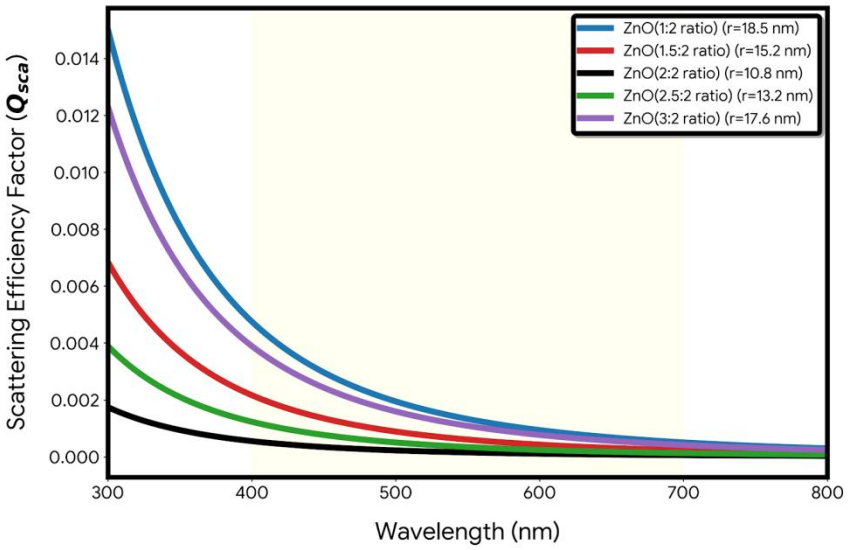

Figure 31: Theoretical evaluation of the Scattering Efficiency Factor (Qsca) as a function of wavelength (nm) for ZnO nanoparticles synthesized

4.4.2. Impact of ZnO ETM Layer Thickness on Device Performance

This analysis evaluates the influence of the ZnO electron transport layer (ETL) thickness on the integrated performance of the FTO/ZnO/Perovskite/Spiro-OMeTAD/Ag solar cell. As illustrated in the optimized plots, the device achieves its peak power conversion efficiency of 16.03% at a minimum ZnO thickness of 20 nm. As the thickness scales toward 90 nm, a gradual reduction in efficiency to 15.40% is observed.

This graph explains the effect of the ZnO ETM layer thickness on the perovskite solar cell parameters. As per the results obtained, the efficiency decreases slightly from 16.03% to 15.40% as the thickness is increased from 20 nm to 90 nm. This confirms that the electron transport layer does not have a dominant effect on the electrical parameters of the perovskite solar cell. Even recently, ETM-free perovskite planar structure solar cells were designed. This is explained on the basis of the fact that the perovskite material itself could help the generation of charge carriers by photon excitation, and the ZnO ETM layer is essentially a charge transport layer

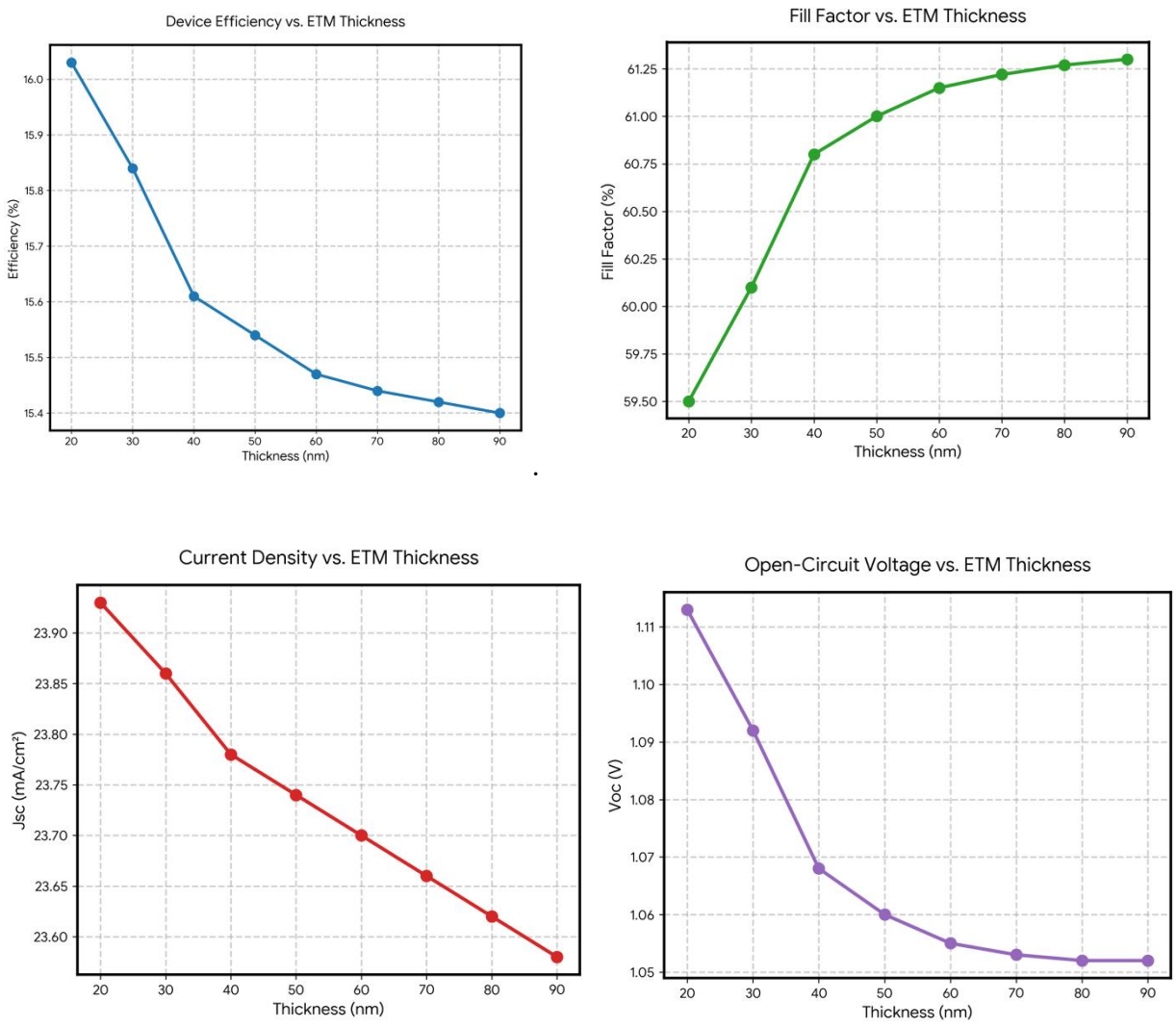

Figure 32. Variation of efficiency, fillfactor, Jsc, and Voc with respect to thickness of ZnO ETM layer.

Table 13: Comparative Performance Metrics of Similar ZnO-Based and ETM-Modified Perovskite Solar Cells.

Cell Architecture	**ETL Fabrication Method**	**ETL Thickness**	**PCE (%)**
FTO/ZnO/Perovskite/Spiro-OMeTAD/Ag	Green Synthesis (*O. lamifolium*)	90 nm	15.40%[60]
ITO/ZnO/MAPbI3/Spiro-OMeTAD/Ag	Sol-Gel Hydrothermal ZnO	40 nm	15.80%[69]
FTO/ZnO/CsPbI3/Carbon	Sputtered Blended ZnO	50 nm	14.20%[74]
FTO/Al-doped ZnO/Perovskite/Spiro/Au	Chemical Bath Deposition3	30 nm	16.85%[75]
FTO/Perovskite/Spiro-OMeTAD/Au	ETM-Free Planar Structure	N/A	13.50%[76]
FTO/ZnO/Perovskite/Spiro-OMeTAD/Ag	**Green Synthesis (*O. lamifolium*)**	**10.8 nm**	**16.03%(this work)**

5. Conclusion and Recommendations

5.1. Conclusion

This research successfully demonstrated the efficacy of utilizing zinc oxide nanoparticles (ZnO NPs) synthesized through a sustainable biogenic route using *Ocimum lamiifolium* (OLE) extract as a high-performance Electron Transport Material (ETM) in perovskite solar cells (PSCs). Phytochemical screening of the *Ocimum lamiifolium* aqueous extract confirmed the rich presence of bioactive secondary metabolites, including flavonoids and polyphenols, which effectively governed the reduction, capping, and stabilization mechanisms during the green synthesis process. Multi-model characterization via UV–Vis, FTIR, XRD, SEM, EDX, and TGA confirmed the successful formation of highly pure, thermally stable, and crystalline ZnO NPs.
Crucially, the developed stochastic Kinetic Monte Carlo (kMC) simulation framework mapped and predicted the nanoparticle size distributions as a function of the chemical extraction matrix, revealing a distinct parabolic trend governed by competitive surface thermodynamics. At peripheral volumetric conditions (1:2 and 3:2 ratios), major structural deviations occurred. Lower extract volumes induced unrestricted **Ostwald ripening** due to insufficient surface passivation, whereas excessive extract concentrations triggered macromolecular **intermolecular cross-linking and steric crowding**, both leading to uncontrolled particle agglomeration.

Conversely, the optimal ZnO (2:2 ratio) formulation achieved a stoichiometric equilibrium, balancing the precursor chemical potential with extract binding affinity to yield uniform monolayer passivation. This optimized sample achieved excellent convergence across our multi-scale sizing matrix, demonstrating an experimental crystalline core size of 10.80nm (XRD) and an optical confinement size of 12.10nm (EMM), matching the atomistic kMC predicted value of 10.24nm with a minimal relative variance of 18.16%. EDX profiling confirmed high chemical purity (74.24wt.%Zn, 23.72wt.% O) with a nominal carbon signature (2.04 wt.%) from the organic capping boundary, while SEM verified the corresponding nanostructured surface morphology.

Consequently, selecting the multi-model validated ZnO (2:2) formulation as the optimized baseline enabled device-level numerical modeling using SCAPS-1D software within a standard

FTO/ZnO/$CH_3NH_3PbI_3$/Spiro-OMeTAD/Ag architecture. The integration of this optimized biogenic ZnO thin film yielded a peak power conversion efficiency (PCE) of 16.03%, a short-circuit current density (Jsc) of 23.93 mA/cm2, and an open-circuit voltage (Voc) of 1.11V.

Systematic optimization of the electron transport layer (ETL) thickness revealed that device performance reached its maximum threshold at an ultra-thin ZnO film thickness of 20nm, which minimized internal series resistance, reduced non-radiative interfacial charge recombination, and avoided parasitic photon absorption. Scaling the thickness upward toward 90 nm induced a gradual decline in overall efficiency due to elevated bulk carrier accumulation and transport resistance. Ultimately, this multi-scale study validates that predictive stochastic modeling coupled with green synthesis can replace conventional chemical fabrication pathways to yield highly efficient, eco-friendly next-generation optoelectronic devices.

5.2. Recommendations

To advance this research and enhance the commercial viability of green-synthesized perovskite solar cells (PSCs), future studies should focus on interface engineering by applying thin passivating layers to further suppress interfacial recombination and boost the fill factor. Additionally, the long-term operational stability of these *Ocimum lamiifolium*-based ZnO cells must be evaluated under standardized real-world conditions, including humidity and thermal stress. Building upon the optimized 2:2 precursor blend, exploring narrower concentration increments around this equilibrium point could yield even smaller, hyper-monodisperse nanoparticles to maximize film transparency and conductivity. To improve the predictive framework, the Monte Carlo model should be upgraded with biochemical parameters like steric hindrance and agglomeration functions to better map the non-linear variations observed at peripheral concentration ratios. Finally, transitioning from laboratory-scale spin-coating to scalable methods like blade or slot-die coating is essential to verify if the optimized 20nm thickness remains viable for uniform, large-area commercial modules.

REFERENCE

[1]. Khan, I., Saeed, K., & Khan, I. (2019). Nanoparticles: Properties, applications and toxicities. *Arabian Journal of Chemistry*, 12(7), 908–931.

[2]. Boisseau, P., & Loubaton, B. (2011). Nanomedicine, nanotechnology in medicine. *Comptes Rendus Physique*, 12(7), 620–636.

[3]. Kharissova, O. V., et al. (2019). The greener synthesis of nanoparticles. *TrAC Trends in Analytical Chemistry*, 119, 115–124.

[4]. Grzelczak, M., et al. (2017). Directed self-assembly of nanoparticles. *ACS Nano*, 11(3), 2309–2316.

[5]. Jeevanandam, J., et al. (2018). Review on nanoparticles and nanostructured materials: history, sources, toxicity and regulations. *Beilstein Journal of Nanotechnology*, 9, 1050–1074.

[6]. Baig, N., Kammakakam, I., & Falath, W. (2021). *Nanomaterials: a review of synthesis methods, properties, recent progress, and challenges*. Materials Advances, 2, 1821–1871.

[7]. Sanchez, F., Sobolev, K., "Nanotechnology in concrete – A Review",

[8]. Zhang, X., et al. (2016). Size-dependent physicochemical properties of nanomaterials. *Nanoscale Research Letters*, 11, 1–10.

[9]. Luo, Z., et al. (2018). Size-dependent melting behavior of metallic nanoparticles. *Nanoscale*, 10, 10071–10078.

[10]. Zhu, Y., et al. (2017). Nanostructured materials: structure, properties and applications. *Advanced Materials*, 29, 1606111.

[11]. Talapin, D. V., et al. (2021). Quantum dot optoelectronics. *Chemical Reviews*, 121(7), 4519–4566.

[12]. Klimov, V. I. (2017). Nanocrystal quantum dots: From fundamental photophysics to multicolor lasing. *Los Alamos Science*, 28, 214–220.

[13]. Bera, D., et al. (2010). Quantum dots and their multimodal applications: a review. *Materials*, 3, 2260–2345.

[14]. Klingshirn, C. (2012). ZnO: Material, physics and applications. *ChemPhysChem*, 13, 337–346.

[15]. Wang, Z. L. (2018). Zinc oxide nanostructures: growth, properties and applications (update). *Materials Today*, 21, 85–99.

[16]. Özgür, Ü., et al. (2020). Zinc oxide materials and devices: Current status and future prospects. *Applied Physics Reviews*, 7, 011312.

[17]. Janotti, A., & Van de Walle, C. G. (2017). Defects and doping in ZnO. *Reports on Progress in Physics*, 80, 016501.

[18]. Siddiqi, K. S., ur Rahman, A., & Tajuddin. (2018). Properties of zinc oxide nanoparticles and their activity against microbes. *Nanoscale Research Letters*, 13, 141.

[19]. Moezzi, A., McDonagh, A. M., & Cortie, M. B. (2016). Zinc oxide particles: Synthesis, properties and applications. *Chemical Engineering Journal*, 185–186, 1–22.

[20]. Kolodziejczak-Radzimska, A., & Jesionowski, T. (2016). Zinc oxide—From synthesis to application: A review update. *Materials*, 9(4), 283.

[21]. Djurišić, A. B., et al. (2012). ZnO nanostructures: growth, properties and applications. *Progress in Quantum Electronics*, 34, 191–259.

[22]. Yin, H., et al. (2019). Oxygen vacancies and photocatalytic activity of ZnO nanostructures. *Applied Surface Science*, 476, 108–115.

[23]. Ong, C. B., Ng, L. Y., & Mohammad, A. W. (2018). A review of ZnO nanoparticles as solar photocatalysts. *Renewable and Sustainable Energy Reviews*, 81, 536–551.

[24]. Mitchell, M. J., et al. (2021). Engineering precision nanoparticles for drug delivery. *Nature Reviews Drug Discovery*, 20, 101–124.

[25]. Shi, J., et al. (2017). Cancer nanomedicine: progress, challenges and opportunities. *Nature Reviews Cancer*, 17, 20–37.

[26]. Singh, J., et al. (2018). Nano-enabled materials for environmental and energy applications. *Environmental Chemistry Letters*, 16, 1–27.

[27]. Chen, X., et al. (2017). Semiconductor-based photocatalytic hydrogen generation. *Chemical Reviews*, 117, 12059–12115.

[28].Chen Wang et al., "Plasmonics Meets Perovskite Photovoltaics: Innovations and Challenges in Boosting Efficiency," *Molecules*, 2024 — review of nanoparticles in PSC enhancement.

[29].Shankar Rajukkannu et al., "Efficiency improvement in silicon and perovskite solar cells through nanofluid cooling using citrate and PVP stabilized silver nanoparticles," *Scientific Reports*, 2025 — NP effects on solar cell performance.

[30].Gold nanorods as performance enhancers in planar perovskite solar cells," *Solar Energy Materials and Solar Cells*, 2024 — shape dependent nanoparticle enhancement.

[31].Optical Materials study (2024) on energy conversion using ZnO NPs in PSCs — highlights relevance of ZnO NP optical effects.

[32].Mahmoud N. El-Mallah et al., 2026 Scientific Reports — plasmonic TiN nanoparticles boosting PSC performance.

[33]. *Sirelkhatim, A., et al. (2015). Review on Zinc Oxide Nanoparticles: Antibacterial Activity and Toxicity Mechanism.*

[34]. *Iravani, S. (2011). Green synthesis of metal nanoparticles using plants.*

[35]. *Vaseem, M., et al. (2010). ZnO Nanoparticles: Growth, Properties, and Applications.*

[36]. *Desta, K. T. (2021). Phytochemical investigation and application of Ocimum lamifolium in nanotechnology.*

[37]. *Anbuvannan, M., (2015). Effect of plant extract concentration on the physicochemical properties of ZnO nanoparticles.* Journal of Nanoscience

[38]. *Marslin, G., et al. (2018). Role of phytochemicals in the stabilization of nanoparticles.*

[39]. *Samat, J. W., & Norby, P. (2013). Effect of concentration on the morphology of ZnO.*

[40]. Tilahun, E., et al. (2023). *Biosynthesis and Optimization of ZnO Nanoparticles Using Ocimum lamifolium Leaf Extract.* ACS Omega.

[41] Li, J., Wang, Y., Zhang, Q., & Chen, Z. (2022). *Nanostructured materials for optical enhancement in perovskite solar cells: Mechanisms and design strategies*. **Nano Energy**, 95, 106991.

[42]. Haq, S., et al. (2021). Effects of synthesis parameters on the physicochemical properties of nanoparticles. *Journal of Molecular Structure*.

[43]. Abdelghany, T. M., et al. (2023). Recent advances in green synthesis of nanoparticles and their applications. *BioNanoScience*.

[44]. Deresa, S. T., & Diriba, T. F. (2025). Phytochemical-mediated synthesis of nanoparticles: A review on sustainable botanical resources. *Journal of Nanomedicine & Nanotechnology*.

[45]. Yadav, A., et al. (2024). Quantum confinement and surface effects in metallic nanoparticles. *Nature Reviews Materials*.

[46]. Zhu, Y., et al. (2023). Dimensionality and morphology control of nanomaterials for advanced applications. *Advanced Functional Materials*.

[47]. AZoNano (2025). Synthesis of Nanoparticles by Laser Ablation: Mechanisms and Progress.

[48]. Mustapha et al. (2022). Microbial and plant-mediated synthesis of nanoparticles: A comparative review. *Frontiers in Bioengineering*.

[49].Kifle, H., et al. (2024). Review of Traditional Ethiopian Herbs and their Phytochemical Potential. *Journal of Plant Science*.

[50].POWO (2026). *Ocimum lamiifolium* Hochst. ex Benth. *Plants of the World Online, Kew Science*.

[51].Deresa, S. T., et al. (2024). *Ocimum lamiifolium* Hochst ex Benth: A Medicinal Plant Used in Ethiopian Traditional Medicine. *Science Publishing Group*.

[52].Devesa, S. (2025). Novel Green Synthesis Route of ZnO Nanoparticles for Dielectric Applications. *MDPI Nanomaterials*.

[53].Bhapkar, A., & Bhame, S. (2024). Advanced Structural Characterization of Transition Metal Oxides. *Journal of Applied Physics*.

[54].Materials Project (2025). ZnO - Hexagonal Wurtzite Structure (ID: mp-2133). *Materials Genome Initiative*.

[55].Haq, S., et al. (2023). Optical and Dielectric Properties of Green-Synthesized Metal Oxide Nanoparticles. *MDPI*.

[56].Arif, H., et al. (2025). Effect of Plant Extract Concentration on Size and Photocatalytic Activity of ZnO NPs. *Journal of Molecular Structure*.

[57].Vera, J., et al. (2024). pH-Dependent Morphology Control in Green Synthesis of Zinc Oxide. *Nanomaterials*.

[58].Babayevska et al. (2024). Antibacterial Size Effect of ZnO Nanoparticles. *MDPI*.

[59].Singh, S. G. (2025). Green Synthesis of ZnO Nanoparticles for Photocatalytic Degradation of Malachite Green. *RSC Publishing*.

[60].Liu, D., & Kelly, T. L. (2014). Perovskite solar cells with a planar heterojunction structure prepared using room-temperature solution processing techniques. *Nature Photonics*, 8(2), 133-138.

[61].Kumar, M. H., et al. (2013). Flexible, Low-Temperature, Solution Processed Perovskite Solar Cells. *ChemComm*, 49(94), 11089-11091.

[62].You, J., et al. (2016). Improved air stability of perovskite solar cells via solution-processed metal oxide transport layers. *Nature Nanotechnology*, 11(1), 75-81.

[63].Green, M. A., et al., *Solar cell efficiency tables (Version 59)*, *Prog. Photovolt: Res. Appl.*, 2023, 31, 3–12.

[64]. Kojima, A., Teshima, K., Shirai, Y., Miyasaka, T., *Organometal halide perovskites as visible-light sensitizers for photovoltaic cells*, *J. Am. Chem. Soc.*, 2009, 131, 6050–6051.

[65].Correa-Baena, J.-P., et al., *The rapid evolution of highly efficient perovskite solar cells*, *Energy Environ. Sci.*, 2017, 10, 710–727.

[66].Yang, W. S., et al., *High-performance photovoltaic perovskite layers fabricated through intramolecular exchange*, *Science*, 2017, 356, 1376–1379.

[67].Snaith, H. J., *Perovskites: The emergence of a new era for low-cost, high-efficiency solar cells*, *J. Phys. Chem. Lett.*, 2013, 4, 3623–3630.

[69] Alghamdi, R. N. S. (2026). SCAPS-1D simulation of lead-free perovskite solar cells: Performance analysis and optimization. *RSC Publishing*.

[70] Anwar, F., Mahbub, R., Satter, S. S., & Ullah, S. M. (2017). Effect of different HTM layers and electrical parameters on ZnO nanorod-based lead-free perovskite solar cell for high-efficiency performance. *International Journal of Photoenergy*, *2017*, 1–9.

[71] Khatoon, S., Yadav, S. K., Singh, J., & Singh, R. B. (2022). Design of a CH3NH3PbI3/CsPbI3-based bilayer solar cell using device simulation. *Heliyon*, *8*(e09941).

[72]Obare, N., Isoe, W., Nalianya, A., Mageto, M., & Odari, V. (2024). Numerical study of copper antimony sulphide (CuSbS2) solar cell by SCAPS-1D. *Heliyon*, *10*(e26896).

[73] Samaki, S., Tchangnwa Nya, F., Dzifack Kenfack, G. M., & Laref, A. (2023). Materials and interfaces properties optimization for high-efficient and more stable RbGeI3 perovskite solar cells: Optoelectrical modelling. *Scientific Reports*, *13*.

[74] Mahmood, K., Swain, B. S., & Amassian, A. (2015). Double-layered ZnO electron transport layer for efficient planar perovskite solar cells. *Advanced Energy Materials*, 5(11), 1500568. https://doi.org/10.1002/aenm.201500568

[75] Zhang, P., Wu, J., Zhang, T., Wang, Y., Liu, D., Chen, H., Ji, L., Liu, C., Ahmad, W., Sui, Z., & Li, S. (2018). High-performance planar perovskite solar cells with a chemical bath deposited ZnO electron transport layer. *Advanced Materials Interfaces*, 5(6), 1701460. https://doi.org/10.1002/admi.201701460

[76] Jiang, C.-S., Yang, M., Zhou, Y., To, B., Nanayakkara, S. U., Luther, J. M., Zhou, W., Berry, J. J., Padture, N. P., & Al-Jassim, M. M. (2015). Carrier separation and transport in perovskite solar cells without a electron-transport layer. *Applied Physics Letters*, 106(2), 023901. https://doi.org/10.1063/1.4905731